SEDIMENTOLOGY the journal of the International Association of Sedimentologists

Sedimentology (2015) **62**, 1408–1445 doi: 10.1111/sed.12188

Sedimentology, three-dimensional geobody reconstruction and carbon dioxide origin of Pleistocene travertine deposits in the Ballık area (south-west Turkey)

HANNES CLAES*, JEROEN SOETE*, KOEN VAN NOTEN†, HAMDY EL DESOUKY*‡, MARCELLE MARQUES ERTHAL*§, FRANK VANHAECKE¶, MEHMET ÖZKUL** and RUDY SWENNEN*

**Geodynamics and Geofluids Research Group, Department of Earth and Environmental Sciences, KU Leuven, Celestijnenlaan 200E, Leuven B-3001, Belgium (E-mail: hannes.claes@ees.kuleuven.be)*
†Seismology-Gravimetry, Royal Observatory of Belgium, Ringlaan 3, Brussels B-1180, Belgium
‡Geology Department, Faculty of Science, Menoufia University, Shebin El-Kom, Menoufia 32512, Egypt
§Petrobras Research Center, Av. Horácio de Macedo Cidade Universitária, 950, Ilha do Fundão, Rio de Janeiro 21941-915, Brazil
¶Department of Analytical Chemistry, Ghent University, Krijgslaan 281-S12, Ghent B-9000, Belgium
***Department of Geological Engineering, Pamukkale University, Kınıklı Campus, Denizli 20070, Turkey*

Associate Editor – John Reijmer

ABSTRACT

The Denizli Basin in the West Anatolian Extensional Province in western Turkey is well-known for its numerous travertine occurrences. A combined sedimentological, diagenetic and geochemical investigation is executed on the Ece and Faber travertines of the Ballık area, the largest travertine site in the Denizli Basin. The first aim of this study is the reconstruction of a three-dimensional geo-model in combination with a detailed sedimentological description from fabric to lithotype, lithofacies and geobody scale, with a focus on integrating pore-typing. The second aim involves the delineation of the CO_2-origin of ancient travertine precipitating waters. Peloidal, phyto and dendritic lithotypes dominate the studied travertines and honeycomb and bacteriform shapes and encrusted bacterial or fungal filaments related to their fabrics suggest a microbial influence. The environment of travertine precipitation evolved from dominantly sub-aqueous, as represented by the sub-horizontal and biostromal reed travertine facies, to dominantly sub-aerial in a thin water film, resulting in the cascade, waterfall and biohermal reed travertine facies. A general progradation of the travertine mound is indicated by the occurrence of stacked waterfall travertines. This results in sigmoidal clinoforms inside a general mound boundary configuration. Strontium and oxygen-carbon isotope signatures of the travertines point to a mixing mechanism of palaeofluids with deeply originated, heavy carbon CO_2 with lighter carbon CO_2 of shallow origin. These deposits can thus be considered as endogenic travertines. Carbonates of the Lycian Nappes acted as main parent carbon source rocks. The relative contribution of the lighter carbon isotopes is most likely to have originated from organic matter or soil CO_2. This study provides a unique three-dimensional insight into the Ballık travertine architecture that potentially can be used as an analogue for subsurface travertine reservoirs worldwide and illustrates the importance of the combined use of $\delta^{13}C$ and $^{87}Sr/^{86}Sr$ signatures in the delineation of the CO_2-origin of travertine precipitating waters.

Keywords 3D geobody architecture, diagenesis, facies, isotope geochemistry, travertine.

INTRODUCTION

The nomenclature of ancient continental spring carbonates often leads to debate, especially considering the terms 'travertine' and 'tufa'. Both types of spring carbonates are formed by precipitation from supersaturated waters caused by the degassing of CO_2. Continental carbonates are classified as 'travertine' when the precipitating water is of hydrothermal origin, while 'tufa' is often related to lower temperature karstic water systems, usually characterized by a higher biotic influence (e.g. Pedley, 1990; Riding, 1991; Ford & Pedley, 1996). However, complications arise, for example where geothermal influence and thus temperature, decreases away from the spring source; this results in proximal travertine and distal tufa, with the exact boundary between them unclear. Furthermore, these systems are often characterized by several springs, resulting in a complex morphology and mixture of facies. Even when the morphology of the deposits with macrophyte content is taken into account, difficulties remain. In areas with strongly fluctuating seasonal temperatures, one spring can be warmer or cooler than the surrounding environment, leading to a difference in degassing mechanisms. This results in different morphologies and travertine or tufa resemblance depending on the season. Furthermore the nomenclature will also be dependent on the scale of observation. Travertine and tufa can thus be considered as end terms of a continuum. This continuum also applies when travertine and tufa are compared with other continental carbonates, as clearly taken into account in the classification schemes of Pedley & Rogerson (2010) and Brasier (2011). Capezzuoli *et al.* (2014) recently proposed the term 'travitufa', for deposits with characteristics between tufa and travertine.

Pentecost (2005), however, excluded the term tufa, and incorporated both tufa and travertine (*sensu stricto*) under travertine (*sensu lato*), for which a classification based on the carrier of CO_2 incorporated in travertine formation was suggested. Meteogene travertines have incorporated CO_2 that can be regarded as meteoric in origin (vegetation, soil and atmosphere), while the CO_2 for thermogene travertines originates from more deeply seated thermal processes (Pentecost, 2005). Thermogene, coming from the Greek terms 'Thermos' and 'Genesis', literally 'Hot' and 'Origin', does not necessarily imply that the travertines were formed from hot fluids, but refers to the deep source of the formation waters. Crossey *et al.* (2006) used the term 'endogenic', for waters containing at least partly deeply derived CO_2, regardless of temperature. The equivalent for purely meteogene travertines (Pentecost, 2005) are epigenic travertines (Crossey *et al.*, 2006). In this contribution the term travertine is always used *sensu lato*, unless explicitly stated otherwise, and classification is based on Crossey *et al.* (2006), differing mainly in linguistic transparency from the nomenclature of Pentecost (2005). The broad use of the term travertine enables the description and discussion of these deposits without drawing premature conclusions towards precipitation conditions such as, for example, water temperature.

Travertine occurrences are known as world heritage sites, such as in Yellowstone National Park, USA (e.g. Fouke, 2011), or in Pamukkale, Turkey (e.g. Kele *et al.*, 2011), but they have also proven useful for society in many other domains. Travertine has been used in numerous small and large constructions as a building stone since Roman times, with the most famous example being the Colosseum in Rome (Italy). Today, travertine is still being quarried intensively and used in construction. Recently, attention to travertines has increased due to their possible application as a climate archive (Yan *et al.*, 2012; Wang *et al.*, 2014), but especially due to their possible occurrence as hydrocarbon reservoirs in offshore Brazil (Terra *et al.*, 2010) and in their African counterparts such as in the Namibe Basin, Angola (Sharp *et al.*, 2013). Seismic data reveal domal aggradational carbonate build-ups (Buckley *et al.*, 2013) and in the Namibe Basin fracture fed mound-like morphologies are linked to fissure ridge and 'dam and cascade' travertines (Sharp *et al.*, 2013). From an exploration point of view, the distribution and extension of different geobodies and their petrophysical properties need to be delineated. However, sedimentological observations in discovered hydrocarbon

reservoirs are limited to core scale and should therefore be extrapolated to a larger context based on field analogue studies.

For all applications, it is important to get a better understanding of the architecture of these carbonate systems, addressing their sedimentology and diagenesis. Two adjacent quarries, i.e. the Faber and Ece quarries situated in the Ballık area in the Denizli Basin (south-west Turkey), were selected based on their excellent large-scale exposure conditions due to active and progressing excavation.

This study is based on extensive field and petrographical observations. An upscaling strategy is followed in the interest of understanding the distribution of the lithofacies within the geobody architecture, to identify which lithotypes dominate the facies, and which fabrics are the building components of the different lithotypes. An important focus lies in discriminating pore-types within the different facies. Based on the fabrics and microstructures, a microbial influence on the fabric formation is evaluated. In addition, the travertines were geochemically characterized by stable oxygen and carbon as well as Sr isotope geochemistry in order to understand the depositional history of these travertine deposits, to decipher the water temperature, to delineate the origin of the Ca^{2+}, HCO_3^--rich precipitating fluids, to determine the source rocks of these carbonate precipitating fluids, and to clarify whether the studied deposits can be considered endogenic or epigenic travertines.

GEOLOGICAL SETTING

The studied Ballık area is situated along the northern graben flank in the south-eastern part of the extensional Denizli Basin (south-west Turkey; Fig. 1). The Denizli Basin is a graben structure *ca* 50 km long and up to *ca* 24 km wide situated at the intersection of the Gediz, Küçük Menderes and Büyük Menderes grabens in the west, and the Baklan and Acigöl grabens in the east. These actively extending basins of the Western Anatolian Extensional Province result from a complex intraplate squeeze-out motion caused by both the northern migration of the Arabian microplate into the eastern Anatolian plate and the rollback subduction of the North African oceanic crust below the Anatolian plate in the Aegean region (e.g. Bozkurt, 2001; Westaway *et al.*, 2005). In the Denizli area, the rollback subduction led to uplift, associated with exhumation and subsequent relaxation, with an extensional collapse, resulting in a horst-graben structure (Westaway, 1993; Westaway *et al.*, 2005; van Hinsbergen *et al.*, 2010; Gürbüz *et al.*, 2012).

Four main groups can be distinguished in the stratigraphic succession of deposits of the Denizli Basin. The main lithologies for these groups, that have been described by several authors (e.g. Collins & Robertson, 1997; Alçiçek *et al.*, 2007; van Hinsbergen *et al.*, 2010), are summarized in the lithostratigraphic section shown in Fig. 2. The first group, that belongs to the Proterozoic–Palaeozoic–Mesozoic rocks of the Menderes Massif and the upper Cretaceous Lycian Nappes (Alçiçek *et al.*, 2007), consists of metamorphic bedrocks that are exposed in the horst structures along the Denizli Basin margins. The amalgamated deposits of the Menderes Massif were metamorphosed into marbles, schists, quartzites, gneisses and phyllites, and recrystallized dolomitic limestones (Alçiçek *et al.*, 2007). The Lycian Nappes in south-west Turkey are subdivided into three units, i.e. the Lycian Thrust Sheets, the Lycian Mélange and the Lycian Ophiolites (Collins & Robertson, 1997, 1998; Sözbilir, 2005; Gündoğan *et al.*, 2008). The main lithologies of these units are dolomitic limestones associated with evaporites, marbles, ophiolitic mélanges and sandstones (Alçiçek *et al.*, 2007). A second group consists of sedimentary rocks of the upper Palaeocene–upper Eocene Dereköy (or Göbeciktepe) unit that lie unconformably on the Lycian Nappes. Rocks in this group are primarily conglomerates, bioclastic limestones, mudstones and sandstone–shale alternations (Sözbilir, 2002). A third group contains the uppermost Oligocene to Neogene sedimentary units, which unconformably overlie the Mesozoic and Dereköy units. These units can be subdivided into two major units, namely the Acıdere and the Denizli or Belevi units, and include recrystallized limestones, conglomerates, sandstones, siltstones and mudstones with lenses of reef carbonates and coal. The Quaternary basin fill is dominated by the Asartepe and Tosunlar Formations and comprises conglomerates, sandstones and mudstones that are locally covered by slope debris, alluvium and alluvial fan deposits, and travertines (Alçiçek *et al.*, 2007), with the last mentioned as the focus of this study.

The Denizli Basin is known for its numerous travertine occurrences (for example, Pamukkale). Earlier studies on travertine in the Denizli Basin

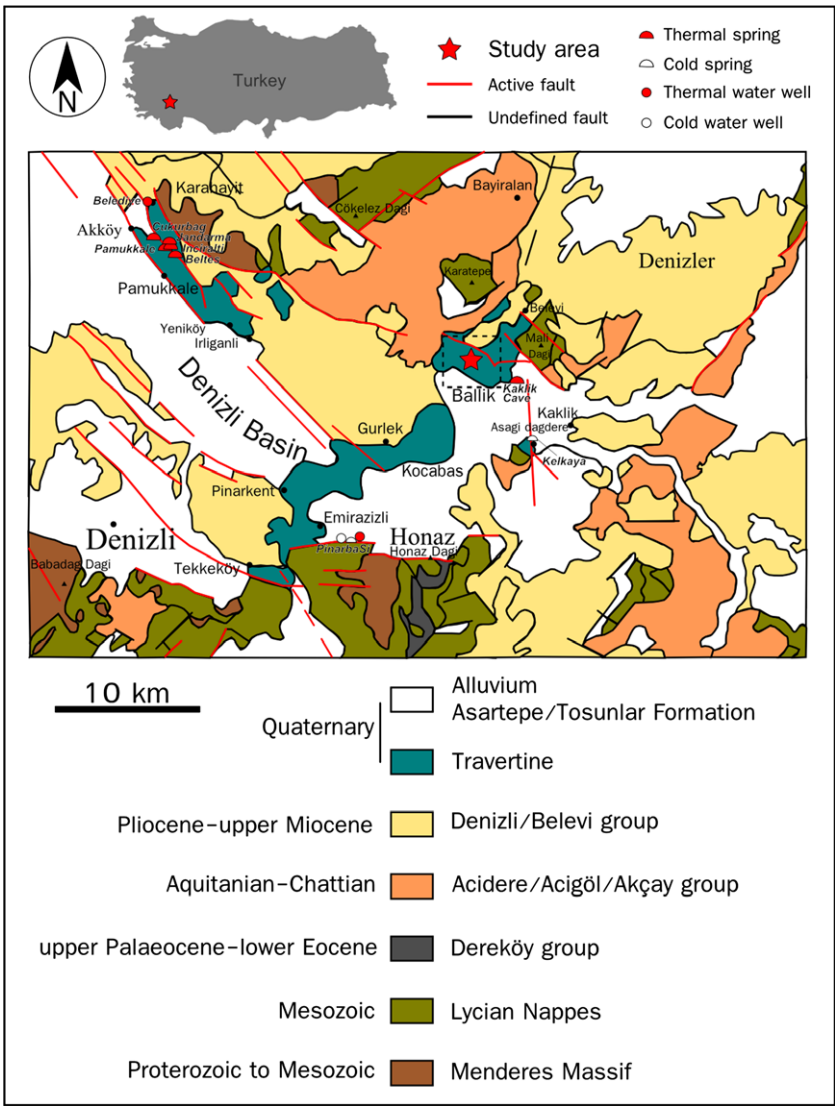

Fig. 1. Geological map of the Denizli Basin, modified from the Geological map of Turkey (Konak & Senel, 2002). The dashed rectangle indicates the location of the zoom on the Ballık area in Fig. 3. Locations of wells and springs from Özkul *et al.* (2013).

focused mainly on modelling the hydrogeology, the geochemical characterization and the potential of geothermal fields in the Büyük Menderes graben (e.g. Şimşek *et al.*, 2005; Kele *et al.*, 2011; Kaypak & Gökkaya, 2012), and on fault, fracture and fissure mapping and their relationship to seismic activity, linking travertine occurrences to the tectonic context of the Denizli area (e.g. Hancock *et al.*, 2000; De Filippis *et al.*, 2012; De Filippis *et al.*, 2013; Van Noten *et al.*, 2013). For the application of travertine as a building stone, geo-mechanical assessments have been executed (e.g. Yagiz, 2006, 2010; Cobanoğlu & Çelik, 2012). The travertines of the Denizli Basin have been dated by thermoluminescence (Engin & Güven, 1997; Özkul *et al.*, 2004), by U series (e.g. Uysal *et al.*, 2007, 2009; Özkul *et al.*, 2013) and by fossil content, such as Pleistocene mammal fossils (Erten *et al.*, 2005) and the *Homo erectus* (Kappelman *et al.*, 2008; Lebatard *et al.*, 2014).

The Ballık area (Fig. 3), which is the focus of this study, was the subject of several previous studies. The occurrence of the Ballık travertine within the structural setting of the Denizli Basin has recently been analysed by Van Noten *et al.* (2013). Based on topography, these authors separated a northern upper area, in which several quarries (more than 10) excavate the south-dipping northern graben flank of the locally east–west trending, Denizli Basin, from a lower 'domal' area, forming a topographical high above the local flat present-day graben floor. The Ece and Faber quarries are part of the domal struc-

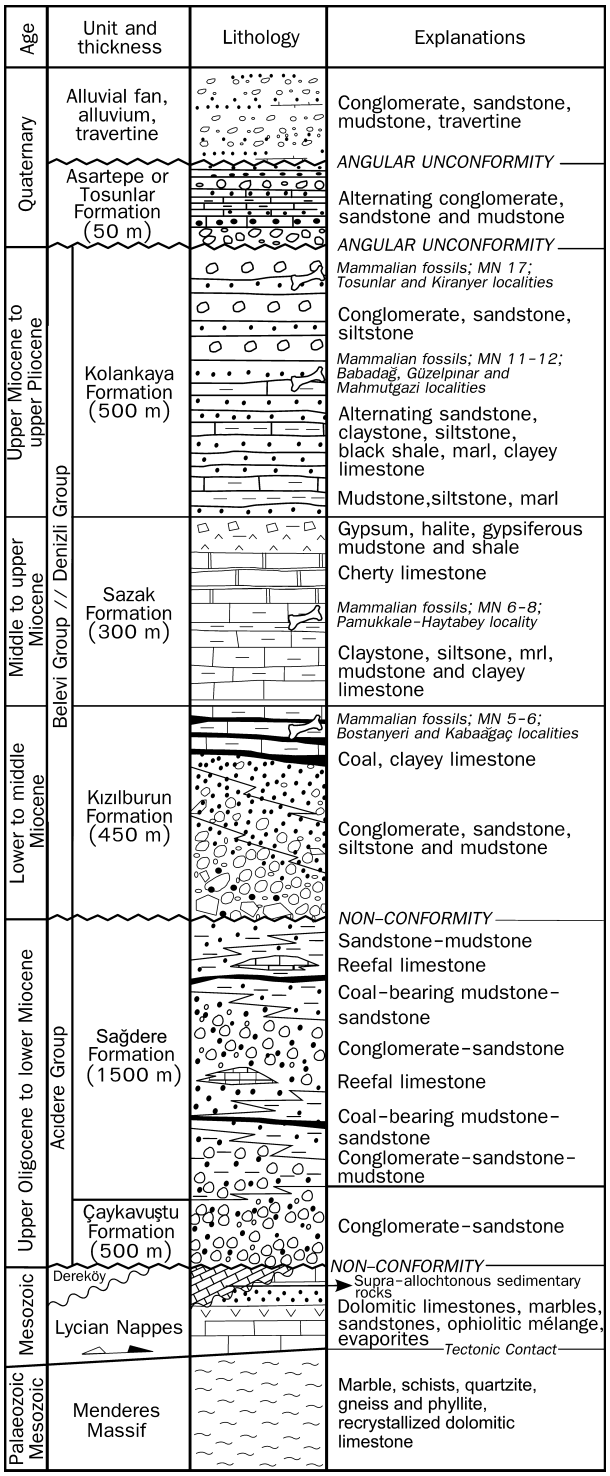

Fig. 2. Lithostratigraphic section of the Denizli Basin (not to scale) based on Sözbilir (2005) and Alçiçek *et al.* (2007).

ture, together with the Çakmak, İlik and Alimoğlu quarries (Fig. 3). Van Noten *et al.* (2013) revealed that the travertine deposits in the studied domal area are affected by multiple fracture generations which resulted from different extension directions that deformed the travertine area. Faults cross-cutting the domal area are interpreted to have formed during north–south extension of the Denizli Basin, and to be subsequently reactivated as result of activity in the adjacent Baklan graben. Currently, the Denizli Basin is still under extension as evidenced by focal mechanism analysis of recent earthquakes (Kaypak & Gökkaya, 2012).

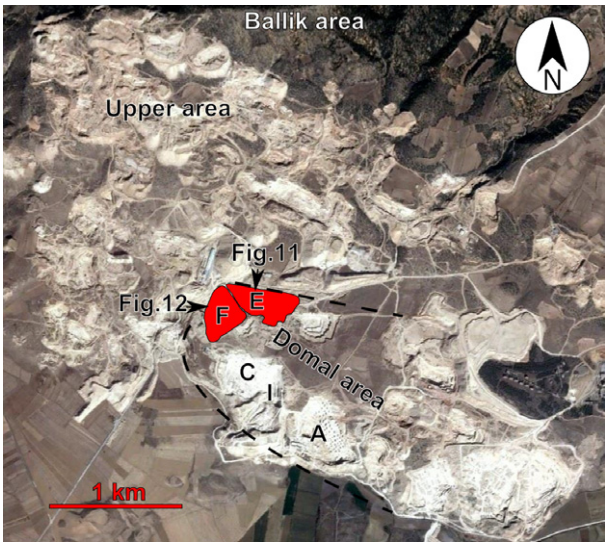

Fig. 3. Satellite image of the Ballık area. The relevant quarries are indicated: E, Ece; F, Faber; C, Çakmak; I, İlık; A, Alimoğlu. The dashed line separates the Domal area from the Upper area. The white areas in the image are both quarries and dumping sites. Modified from Google Earth. (c) 2014 Basarsoft. Image (c) 2014 CNES/Astrium.

Dating of the *Homo erectus* fossil and pebbles from conglomeratic levels in combination with magnetic susceptibility on samples from the Faber quarry, resulted in a proposed minimum age of 1·1 Ma for the end of massive travertine deposition and a maximum age of 1·78 Ma for travertines 15 m below the present excavation level of the Faber quarry (Lebatard *et al.*, 2014). The age data of Lebatard *et al.* (2014) are in contrast with the thermoluminescence dating of the Ballık travertines of 828 ± 93 ka (Engin & Güven, 1997) and 490 ± 50 ka (Özkul *et al.*, 2004). Lebatard *et al.* (2014) also provided stable isotope data and porosity data of a stratigraphic section in the Faber quarry; unfortunately the data were not linked to the lithofacies or lithotype of the samples.

Özkul *et al.* (2002, 2013) provided a concise general macroscopic and microscopic description of the Denizli travertines in combination with stable isotopic data and a stratigraphic section of the İlik quarry (Fig. 3). Khatib *et al.* (2014) performed a mineralogical and sedimentological analysis of the Faber quarry, but focused mainly on the non-travertine lithologies in the frame of palaeomagnetic dating. These authors did, however, perform X-ray diffraction (XRD) analyses on the travertines which show a 97 to 99% calcite and 1 to 3% silica mineralogy. El Desouky *et al.* (2015) focused on the cement phases in the travertines of the Çakmak quarry using microthermometry on fluid inclusions and Sr isotopes to constrain the origin of the travertine fluid flow system. The most proximal active continental carbonate precipitation to the study area takes place in the Kaklik cave, which locally is referred to as 'Subsurface Pamukkale', just south-east of the Ballık area (Fig. 1). The present-day temperature of this thermal spring is 22·8°C (Özkul *et al.*, 2013). The hottest thermal spring in the Denizli Basin is the Çukurbağ spring (57·1°C) on the Pamukkale site (Fig. 1; Özkul *et al.*, 2013).

METHODOLOGY

Upscaling, field mapping and sampling

The sedimentological observations and subsequent interpretations of the Faber and Ece travertines will be presented following an upscaling philosophy, providing information from fabric to lithotype, to lithofacies, to geobody scale:

"*A sedimentary facies or lithofacies is a mass of sedimentary rock which can be defined and distinguished from another by its geometry, lithology, sedimentary structures, palaeocurrent pattern and fossils. It reflects a depositional environment that is preserved in the stratigraphic record in the form of a facies.*" (Selley, 1985)

A 'facies' thus groups all features that allow delineation of a large-scale depositional setting in the travertine body. Each facies is characterized by a set of lithotypes defining the macroscale appearance of the microfabric organization. Some lithotypes can be part of different facies, whereas others may be facies specific. It is the combination of several lithotypes that makes up a facies. This approach was first described for the Upper Pleistocene travertines of Rapolano Terme (Italy) by Guo & Riding (1998) and is here adapted to the studied travertines.

This study relies on detailed field observations made in the two adjacent quarries, Faber and Ece, with quarry dimensions of *ca* 200 m wide by *ca* 400 m long and *ca* 70 m in height. Detailed photographs of all the quarry walls of the different excavation levels were printed, and used in the field as background pictures for detailed line-drawings of the lithofacies. These line-drawings allowed assessment of the thickness and lateral continuity of the lithofacies and intra-facies (lithotype) variations.

In each quarry, two vertical sections were mapped in detail and sampled. Three samples were collected per excavation level, which resulted in a sample density of one sample every 2 to 3 m, or *ca* 50 samples in each quarry. Additional samples were collected to include the whole travertine variability.

Based on the detailed drawings of the quarry walls and on the sampled sections, an overall 3D geobody facies distribution has been constructed. To gain better insight into the spatial distribution of the facies, line drawings were projected on the quarry walls using 3D drawing software (SketchUp; Trimble Navigation Limited, Sunnyvale, CA, USA).

Petrography

Because of the fragility of travertine, particularly at pore edges, the samples were doubly impregnated with resin before thin-section preparation. A fluorescent dye was used in order to easily distinguish (micro-)porosity with fluorescent light microscopy. Petrographic characterization was conducted on an Olympus BX60 (Olympus Corporation, Tokyo, Japan) and Leica (Leica Microsystems, Wetzlar, Germany) DM LP Parallel and Crossed Polar Optical and Fluorescence microscope (PPM, CPM and FM, respectively). A Nikon Optiphot with a Modified Technosin Model 8200 MkII stage microscope (Nikon Corporation, Tokyo, Japan) was used for Cold Cathodoluminescence (CCL) observations. Use of a JEOL JSM-6400 Scanning Electron Microscope (SEM; JEOL Ltd, Tokyo, Japan) and a Philips XL30 Environmental SEM (E-SEM; Philips, Eindhoven, The Netherlands) allowed observations with magnifications up to 11 000×.

Rubidium–strontium analyses

The Rb and Sr contents and the $^{87}Rb/^{86}Sr$ and $^{87}Sr/^{86}Sr$ ratios were determined for 12 represen-

tative travertine samples. The Rb-Sr analyses were performed at the Department of Analytical Chemistry, Ghent University (Belgium). Carbonate powders were obtained using a dental drill and were dissolved in 6 M HCl on a hotplate. The digests were subsequently evaporated to dryness and redissolved in 7 M HNO_3. The Rb and Sr concentrations were determined using a Thermo Scientific XSeries 2 quadrupole-based ICP-MS (Thermo Fisher Scientific Inc., Waltham, MA, USA) instrument using external calibration combined with Yttrium as an internal standard (Vanhaecke *et al.*, 1992). The $^{87}Rb/^{86}Sr$ ratios were calculated following the procedures described by Vanhaecke *et al.* (1999). Strontium was isolated from the sample matrix using a Sr spec™ resin, following the isolation procedure described by De Muynck *et al.* (2009). The Sr isotope ratio measurements were carried out using a Thermo Scientific Neptune MC-ICP-MS instrument. The intensities obtained for ^{83}Kr and ^{85}Rb were used to correct for isobaric interference from Kr and Rb. The Sr isotope ratio data were internally corrected for instrumental mass discrimination based on the accepted $^{86}Sr/^{88}Sr$ ratio of 0·1194. Blank Sr signals were negligible compared to the Sr intensities encountered for samples and standards. Repeated analyses of the Sr carbonate isotopic Standard Reference Material number 987 from the National Institute of Standards and Technology USA (NIST SRM 987 CaCO3) over the duration of this study yielded an average $^{87}Sr/^{86}Sr$ ratio of 0·710271 ± 0·000023 (n = 42), which is well in agreement with the accepted $^{87}Sr/^{86}Sr$ ratio of 0·710248 for this material (Thirlwall, 1991).

Stable oxygen and carbon isotopes

Avoiding apparent existing cement phases, 109 travertine samples were obtained using a dental drill. Stable oxygen and carbon isotopic signatures of the samples were determined at the 'Friedrich-Alexander-Universität' (Erlangen-Nürnberg, Germany). Carbonate powders were reacted with 100% phosphoric acid at 70°C in a Gasbench II connected to a ThermoFinnigan Five Plus mass spectrometer (Thermo Scientific Inc.). All values are reported in per mil (‰), relative to Vienna Pee Dee Belemnite (V-PDB) by assigning a $\delta^{13}C$ value of +1·95‰ and a $\delta^{18}O$ value of −2·20‰ to the standard NBS19. The analytical standard deviations for $\delta^{13}C$ and $\delta^{18}O$ are 0·04‰ and 0·05‰, respectively.

RESULTS

Lithotypes, lithofacies distribution and geobody architecture

Names, characteristic features and fabrics of the main distinguished lithotypes are listed in Table 1 and are illustrated in Figs 4 and 5. Peloidal, dendritic and phyto travertine lithotypes dominate the Ece and Faber travertines. It is important to stress that similar fabrics can occur in different lithotypes. Peloidal micrite, for example, is typical for the peloidal lithotypes but is also one of the main fabrics of the micritic dendrites. Dendrites in turn dominate the dendritic lithotypes, but also occur in the phyto lithotypes around mouldic pores and in the coated grain lithotypes.

The lithotypes can be distinguished from a hand specimen or core sample. Based on the proportion and association of specific lithotypes, they subsequently can be related to one of the four dominant Ece and Faber travertine lithofacies. The sub-horizontal (Fig. 6), reed (Fig. 7), cascade (Fig. 8) and waterfall travertine facies (Fig. 9) are described in detail in Table 2. Additionally several external sediment inputs were observed in the form of marly to polymictic conglomerate layers (Fig. 10) and are briefly described in the next paragraph.

The lithofacies were mapped based on observations on quarry walls (Figs 11 to 13) and further characterized in detail based on stratigraphic sections (for example, Fig. 14). This information was subsequently projected onto a 3D reconstruction of the quarry walls (Fig. 15). Based on facies occurrences, their distribution, slope and architecture, all facies were extrapolated in the area where travertine is already excavated or where no outcrop information is available. There is an absence of faults in the Ece quarry. In the Faber quarry two faults are recognized (Figs 12 and 15). Due to the steeply dipping orientation and the limited displacement (*ca* 0·5 m) of these strike-slip faults (Van Noten *et al.*, 2013), their influence on the facies distribution is negligible. The resulting 3D model shows the variability in facies distribution, their extension and the geobody architecture. An advantage of the 3D model is that different sections in all directions can be reconstructed (for example, Fig. 16).

The sections, maps and 3D model show that the aggradational sub-horizontal facies is present in the lower part of both quarries, extend-

Table 1. Overview of the Ece and Faber travertine lithotypes with description of fabrics and characteristic features.

Lithotypes	Description (including fabric organization)	Associated pore type	Figure on macro-scale	Figure on micro-scale	SEM-figures
Dark coloured peloidal travertine	Amalgamated and almost non-translucent micritic carbonate spheroids (*ca* 60 to 100 µm in diameter), i.e. peloidal micrite components, are surrounded, intercalated or covered by micrites and/or (micro-)sparites. The micrites are enriched in organic matter, in contrast to the surrounding cloudy micrite phases and especially the transparent sparites. The sparites between the peloids readily transmit light, what gives them, depending on their crystallinity, a beige to brownish macro-appearance. They thus, when dominantly present, result in a **'Dark coloured peloidal travertine'** lithotype. The organic-rich almost non-translucent micrite fabrics disperse almost all light and thus result in a white macro-appearance. When they dominate the peloidal travertine, they result in a **'Light coloured peloidal travertine'** lithotype.	Interpeloidal pores are typically in the order of 10 to 100 µm, but can be up to millimetre-size. On a macro-scale this porosity type often follows lamination and resembles fenestral porosity, hence 'pseudo-fenestral porosity'.	Figs 4D and 6	Fig. 4A	Bladed spars reduce pore space and appear as flowers of sparhead crystals under the SEM: Fig. 5A and B
Light coloured peloidal travertine				Fig. 4B	
Micritic dendritic travertine	Micritic Dendrites are built of organic-rich non-translucent dendritic micrite, which is often coated by an isopachous microsparite layer. Individual dendrites (in 2D cross-section) contain multiple branches starting from the same point. Secondary branches are uncommon. Length to width ratios of the dendrites usually vary around two, with typical widths in the order of 500 to 1000 µm. When individual micritic dendrite units can be distinguished on macro-scale, lithologies are classified as a **'Micritic dendrite travertine'** lithotype. The micritic dendrite travertine usually consists of branching peloidal micrite. When they form dense lamina with macroscopic crust appearance, they are classified as **'Dendrite crust travertine'**. These crusts consists of morphologies ranging from peloidal micrite to more vertically elongated organic-rich fibrous micrite. A microscopic lamination is sometimes present. Both of these endmembers, but particularly the latter, can show an undulose extinction of the micrites under crossed polars, indicative of, possibly ongoing, recrystallization.	Inter-dendrite pores and a distinct presence of intra-dendrite microporosity. SEM observations show up to 100 µm-size poretubes. On macro-scale, the crusts are associated with interlayer porosity.	Figs 4H, 6 and 8D	Fig. 4E	SEM: 100 µm-sized poretubes in the dendritic fabrics (Fig. 5C and D), with on their edges rod-shaped micrometre spheresrods (Fig. 5E) that are closely associated with honeycomb textures (Fig. 5F) and bacteriform spheres (Fig. 5G). Some bacterial or fungal filaments were also observed (Fig. 5H)
Dendrite crust travertine				Fig. 4F-G, Fig. 17I	
Crystalline dendrite travertine	Crystalline dendrites are completely crystalline. Their dendritic morphology and/or crystal edges are marked by dark inclusions or micrite. When dense packing prohibits distinguishing macroscopic individual dendrite units (i.e. **'Crystalline dendrite travertine'**), they are classified as **'Crystalline band travertine'**. Due to their crystallinity and the presence of dark inclusions, they appear macroscopically as darker, up to several centimetre thick, laminae. A microscopic lamination is often apparent similar to the micritic dendrite travertines, probably representing growth layers.	Interdendrite porosity	Fig. 4J	Fig. 4I	/
Crystalline band travertine		Low to non-porous	Fig. 4L	Fig. 4K	/

Table 1. (continued).

Lithotypes	Description (including fabric organization)	Associated pore type	Figure on macro-scale	Figure on micro-scale	SEM-figures
Bryo phyto travertine	These lithotypes are characterised by a high mouldic porosity, resulting from calcite encrustation (or trapping) and subsequent decay of plants that served as substrates. Three sub-lithotypes are differentiated based on the type of plant.Complex networks of millimetre-sized tubular mouldic pores result from bryophyte encrustation and decay, hence **'Bryo phyto travertine'**. The sporophytes of these bryophytes can also result in mouldic pores. Further distinction is mainly based on the size of the plant moulds. Grass has a diameter smaller than 2 mm, whereas the diameter for reed varies between 0.2 cm and 1 cm, hence **'Grass phyto travertine'** and **'Reed phyto travertine'**, respectively. The pores are typically rod-like, i.e. they display a one dimensional habit. Often grass moulds are vertically parallelly aligned. Large plant moulds, e.g. related to branches were not included due to the larger scale on which they occur, outpacing the lithotype classification scale. When different plant types occur, the sample is classified according to the macroscopically most dominant plant-type. Furthermore, depending on the dominance of the plants or the matrix, the lithotypes can be marked as matrix-dominated or phyto-dominated. Macroscopically, this results in cement reduced plant phyto moulds that are accentuated by thin white coatings, inside the darker beige matrix. Moulds can result from plants in eroded or growth position. The phyto lithotypes have a typical microfabric arrangement (e.g. Fig. 4R): Mouldic pores form the central point of radial dendritic organic-rich micritic overgrowths. These radial dendrites are amalgamated by sparite coalesced peloidal micrite. Bladed sparites often reduce the mouldic pore space. Even when the dendrite overgrowth is missing, the organic rich peloidal micrite that coated the plants accentuates the moulds.	Plant moulds (should not be mistaken for charophyte moulds e.g. Fig. 4T)	Fig. 4N	Fig. 4R	Fig. 4M
Grass phyto travertine			Fig. 4P		Fig. 4O
Reed phyto travertine			Figs 4S and 7		Fig. 4Q, R
Monomictic travertine	For **'Monomictic travertine'**, fragments consist exclusively of travertine composition, usually floating in a peloidal micritic carbonate matrix, and could thus be classified as an intraclastic rudstone to breccia. The fragments are millimetre to decimetre sized, and vary from angular to sub-angular to even sub-rounded. **'Polymictic travertine'** consists of fragments of variegated mineralogy including quartz, feldspars, travertine, non-travertine carbonate, metamorphic minerals and iron oxides/hydroxides that are embedded in a micritic carbonate matrix. Fragments range from sub-millimetre to multiple centimetre-scale and are dominantly rounded. Depending on the dominance of carbonate precipitation versus extraclast input the deposits can be classified as an extraclast rudstone or evolves to a (non-travertine) conglomerate.	Porosity of the monomictic travertines depends on the nature of the travertine clasts. However, due to the relatively massive matrix (some interpeloidal porosity), they generally possess a low porosity.	Figs 4V and 8G	Fig. 4U	/
Polymictic travertine		Porosity of the polymictic travertines is generally low, but strongly depends on the kind of pebbles, the relative abundance of matrix and pebbles, the sorting and packing of the pebbles and the degree of cementation.	Fig. 4X	Fig. 4W	/

Table 1. Continued.

Lithotypes	Description (including fabric organization)	Associated pore type	Figure on macro-scale	Figure on micro-scale	SEM-figures
Coated grain travertine	**'Coated grain travertine'** is travertine that is dominated by coated grains. Based on the size of the grains and their internal structure, these can be classified as peloids, ooids, pisoids and oncoids (analogue to marine carbonates). Their cores can be both lithoclasts of travertine and non-travertine lithologies, as well as bioclasts. Beside the classical coated grains, radial dendritic structures were observed for the Faber and Ece travertines showing a sweeping cross-extinction under crossed polars. They sometimes show a concentric microscopic lamination comparable to that observed in the dendritic lithotypes.	Depending on the size and type of the grains, porosity varies. Intraparticle porosity is generally low. Interparticle porosity can be absent for particles floating in a matrix, or can be reduced or completely occluded by cementation. For larger particles (>2 mm), however, interparticle porosity is maintained.	Macroscopically, these radial dendrites will usually appear white, in a (slightly) darker matrix: Fig. 4AB. Pisoids: Fig. 8F	Radial dendrites: Fig. 4Y to AA. When these radial dendrites have a thin-laminated coat, they can be classified as pisoids: Fig. 4Y Chafetz & Folk (1984) refer to them as pisoids, even when no coating is present.	/
Gastropod travertine	**'Gastropod travertine'** is travertine dominated by gastropods. These travertines often show a darker, brownish colour, probably related to their higher non-carbonate content.	Inter and intra-gastropod porosity is often almost completely reduced, while gastropod-mouldic porosity is almost not reduced.	Fig. 4AD	Fig. 4AC	/
Raft travertine	**'Raft travertine'** is travertine dominated by rafts. Delicate, brittle, grey to pale brown, sub-horizontally aligned crystalline plates, which can also occur as amalgamated flakes.	Depending on their organization, these structures can lead to very high porosities. The cementation of these plates or flakes is two-fold. It reduces pore space, but also strengthens their structure promoting pore space preservation counteracting compaction.	Fig. 4AF	Fig. 4AE	/

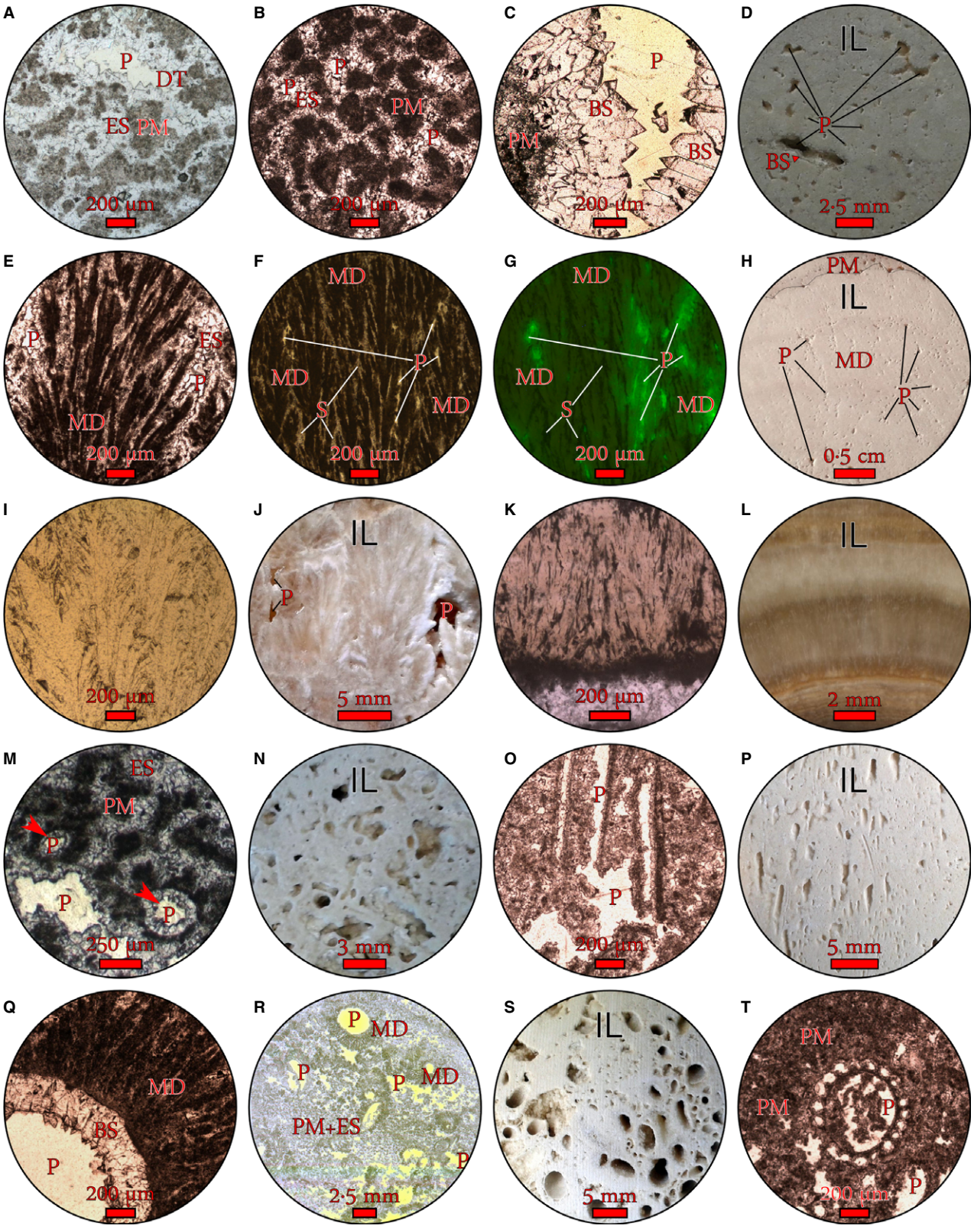
A
P
DT
ES PM
200 µm
B
P
P
ES
PM
P
200 µm
C
P
BS
PM
BS
200 µm
D
IL
P
BS
2·5 mm
E
P
ES
P
MD
200 µm
F
MD
P
MD
S
MD
200 µm
G
MD
P
MD
S
MD
200 µm
H
PM
IL
P
MD
P
0·5 cm
I
200 µm
J
IL
P
P
5 mm
K
200 µm
L
IL
2 mm
M
ES
PM
P
P
P
250 µm
N
IL
3 mm
O
P
P
200 µm
P
IL
5 mm
Q
MD
BS
P
200 µm
R
P
MD
P
P
MD
PM+ES
P
2·5 mm
S
IL
5 mm
T
PM
PM
P
200 µm
P

Fig. 4.

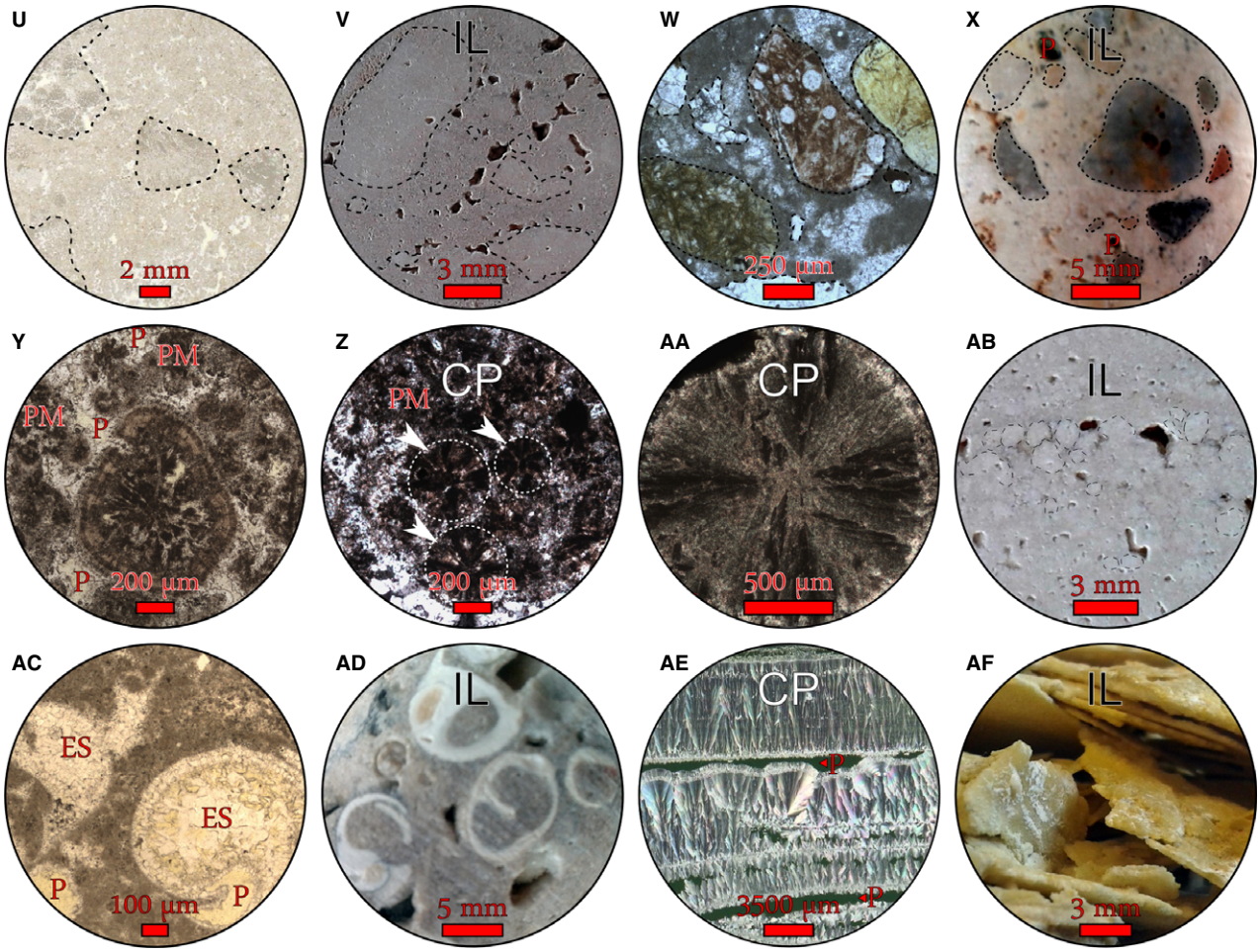

Fig. 4. Photomicrographs of the Ece and Faber lithotypes (P, pore; S, spar; ES, equant spar; BS, bladed spar; DT, dog tooth spar; PM, peloidal micrite; MD, micritic dendrite; IL, incident light; CP, crossed polars). (A) Dark coloured peloidal travertine. (B) Light coloured peloidal travertine. (C) Bladed spars (up to 100 µm long) at pore edge inside light coloured peloidal travertine. (D) Macroscopic appearance of peloidal micrite with pseudo-fenestral interpeloidal porosity. (E) Micritic dendrite travertine. (F) Dendrite crust travertine. (G) Fluorescence micrograph image of the dendrite crust travertine in (F). (H) Macroscopic very white appearance of the dendrite crust travertine. (I) Crystalline dendrite travertine. (J) Macroscopic example of crystalline dendrites. (K) Crystalline band travertine. (L) Macroscopic appearance of crystalline band travertine. (M) Bryophyte moulds in bryophyte travertine. (N) Macroscopic appearance of bryophyte travertine. (O) Grass moulds in grass phytotravertine. (P) Macroscopic appearance of grass phyto travertine. (Q) Bladed cements reducing porosity of a reed mould surrounded by radial micritic dendrites in reed phyto travertine. (R) Typical fabric arrangement for phyto lithotypes, in this case a reed phyto travertine. (S) Macroscopic appearance of reed phyto travertine. (T) Charophyte mould in a peloidal micrte matrix. (U) Monomictic travertine under PPL. (V) Macroscopic appearance of monomictic travertine. (W) Polymictic travertine under PPL. (X) Macroscopic appearance of polymictic travertine. (Y) Radial dendrite coated grain travertine. (Z) Radial dendrite coated grains in peloidal micrite matrix. (AA) Radial dendrite coated grain with a cross-shaped undulous extinction under crossed polars. (AB) Macroscopic appearance of the radial dendrites as white spheres in a slightly darker matrix. (AC) Gastropod travertine. (AD) Gastropod travertine, in this case associated with a darker, greyish matrix. (AE) Cementation enforced raft travertine. (AF) Macroscopic appearance of raft travertine.

ing at least 200 by 400 m, with a minimal thickness of 7 m. It is covered first by the biostromal reed facies with more plant growth locally, as observed in the Ece quarry (Fig. 11). The geobody vertically changes into a sloping system first with a gently crenulating, crinkly steady sloping cascade facies, evolving into a steeper sloping cascade facies and a strongly

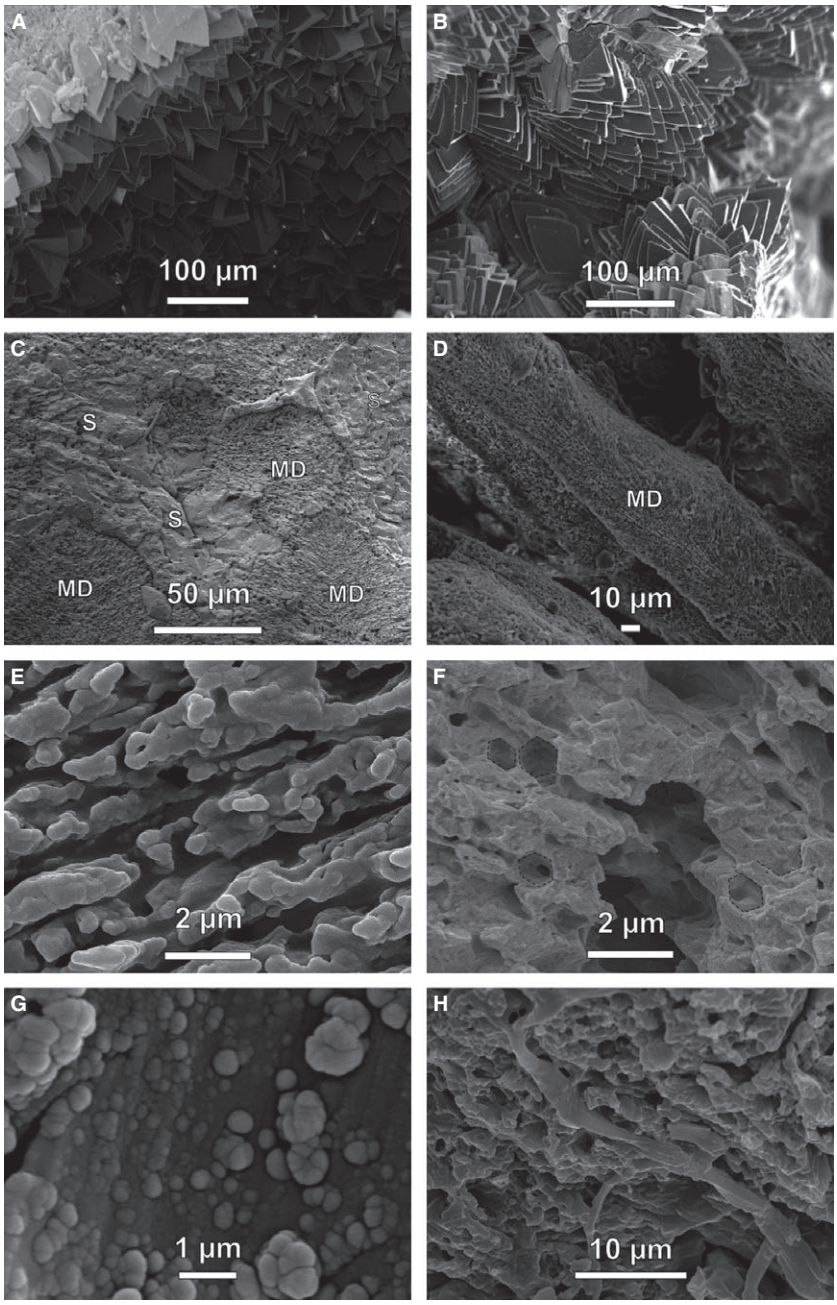

Fig. 5. (E-)SEM micrographs. (A) Spearhead cement spars with straight crystal surfaces. (B) Spearhead cement spars with curved crystal surfaces, i.e. gothic arch crystals *sensu* Folk *et al.* (1985). (C) Micritic dendrite bushes (MD) surrounded by spars (S). (D) 100 µm sized pore tubes between micritic dendrite branches (MD) which also show microporosity. (E) Microporous character of the micritic dendrites with rod shapes on the edges possibly related to dissolution. (F) Associated (honeycomb) alveolar textures of the dendritic fabrics. (G) Bacteriform spheres. (H) Encrusted bacterial or fungal filament on alveolar structures.

irregular steep sloping waterfall facies. Cascade travertines consist of isopachous beds, while the waterfall beds are anisopachous and even discontinuous, associated with primary cave systems. The sloping travertines are the dominant facies in the Ece and Faber quarries. The cascade facies, for example, extends over more than 200 by 400 m, with a thickness of 15 to 30 m. The internal complex morphologies of the sloping facies are related to the changing flow path of the down-flowing water during precipitation; this results in lateral changes from waterfall bodies to cascade and reed travertines, for example at the top of the Faber quarry (Fig. 12). Despite these complex morphologies, some clear systematic patterns exist. The general dip of the slopes from the cascade and waterfall facies travertines is to the north-west. The up to 20 m thick waterfall travertine facies can be followed over the two quarries, and shows a pronounced prograding trend. On top of the waterfall facies, the decreasing steepness again results in cascade travertines. The reed travertine facies subsequently levels up the sys-

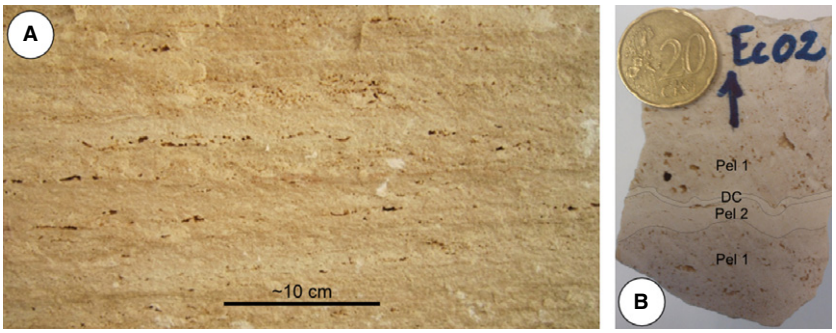

Fig. 6. (A) Sub-horizontal travertine facies with layer parallel pseudo-fenestral porosity. (B) Hand specimen of the sub-horizontal travertine facies with the main lithotypes, i.e. dark and light peloidal micrite and dendritic crust travertine (Pel1, Pel2 and DC, respectively). Coin for scale (22·25 mm diameter).

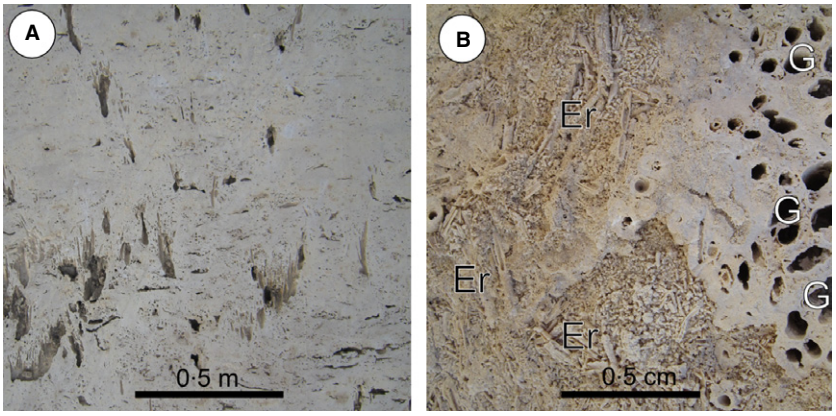

Fig. 7. (A) Reed facies with illustration of a mould of reed in growth position. Note also the eroded or fragmented plant mouldic porosity between the reeds in growth position. (B) Top view of both eroded encrusted plants (Er) and the vertical moulds resulting from reeds in growth position (G).

tem and locally occurs as patchy distributed decametre-scale individual biohermal bodies. The upper aggradational biostromal levelling up reed sequence has a lateral extension over more than 200 m with a thickness between 1 m and 20 m. Local precipitation pauses resulted in temporal erosional surfaces and even immature soil formation.

Lateral non-travertine lithologies

Three different marl to marl-conglomeratic occurrences were mapped. The first occurrence is observed in the Faber quarry as a well-developed package covering the sub-horizontal travertine facies. This occurrence has a maximum thickness of *ca* 17·5 m, in the western part of the quarry, and thins out to a thickness of *ca* 8 m in the eastern part of the quarry, i.e. over a distance of *ca* 170 m. It consists of an alternation of conglomerates and marls (Fig. 10B) and locally some travertine beds with a considerable siliciclastic grain content (more than 15%). The marls, which are the dominant lithology, vary from dark beige to brown and show root traces. Root traces point to a shallow to subaerial depositional environment, with an increased input of fine-grained detritus. The conglomerates show decimetre-scale erosional bases reflecting multiple channels of heterogeneously sized deposits (Fig. 10C); they vary from clast-supported to matrix-supported. Clasts are well-rounded with diameters of less than 1 cm, to often more than 10 cm (Fig. 10B), and regularly show an imbricated organization. The clasts consist of quartz, feldspars, non-travertine carbonates, and travertines. Also volcanic and metamorphic clasts (mainly marble) and minerals (for example, pyroxenes, and possibly some muscovite and garnet) and iron oxides and hydroxides were observed. The onset of renewed travertine formation is transitional, resulting in a centimetre-bedded marl to travertine intermediate lithology.

A second non-travertine unit is found along the flanks of the dome, in the south-western part of the Faber quarry and the northern flank of Ece, where it locally interfingers with the cascade travertine facies. This facies dominantly consists of grey-green coloured marls and clays to claystones that have a very homogeneous outline. Clays sometimes show a millimetre-scale to centimetre-scale lighter and darker lamination (Fig. 10A); they also have a high gastropod content. The top of the travertine body is covered

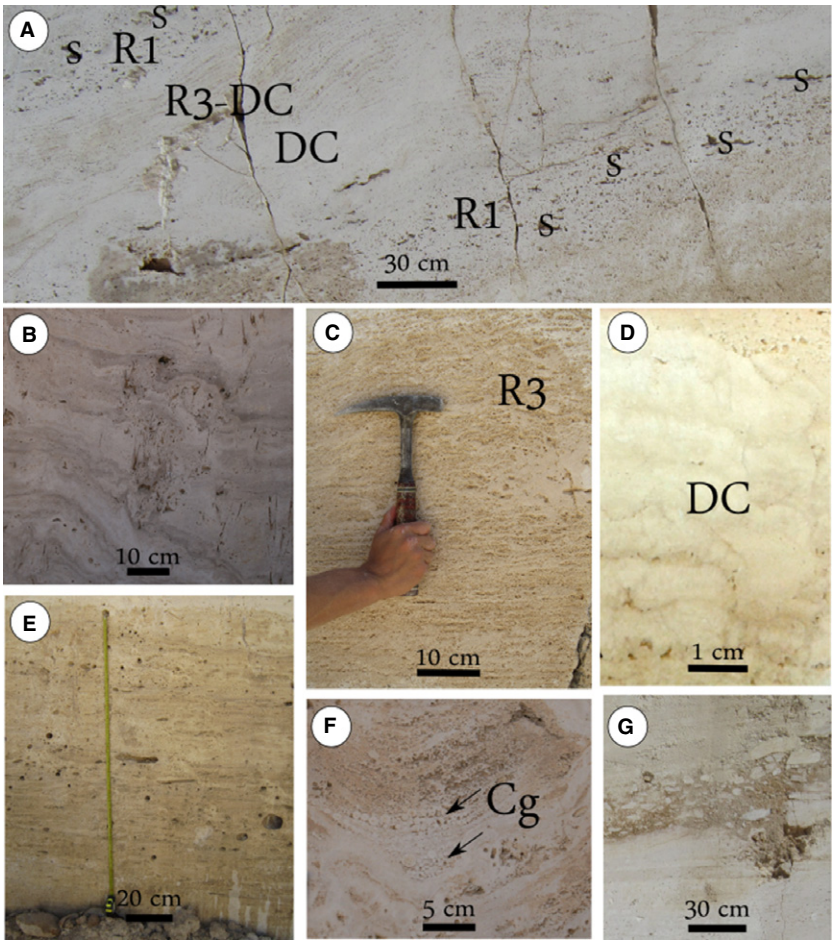

Fig. 8. Field views of the cascade facies and associated lithotypes (R1, reed phyto travertine; S, shelter porosity; R3, bryophyte travertine; DC, dendrite crust travertine; Cg, coated grains). (A) Cascade facies with alternation of centimetre-thick units of different lithotypes. Reed phyto-travertine with some small-scale shelter-porosity leads to high porosities. Bryophyte travertines and especially the dendritic crust travertines have a lower macro-porosity. (B) Occurrence of reed moulds delineating a triangular configuration giving rise to small palaeotopographic elevations. (C) Dominantly bryophyte travertine lithotype. (D) Macroscopically dense, white dendrite crust travertine. (E) Cascade facies with beige to brown plant mouldic (grass-reed-branch) rich units. (F) Occurrence of coated grains (Cg) in bowl-shaped small depression. (G) Monomictic travertine lithotype, with fragments in a red-brown clayey semi-consolidated matrix.

by a third marl-conglomerate occurrence (Fig. 10D), which consists of marls, grading upward into polymictic conglomerates with clasts varying in size between granules and boulders, coarse sandy layers showing unidirectional low-angle cross-bedding, and some minor clays.

Porosity and diagenesis

As mentioned in Table 1, several pore types characterize the different lithotypes. Pseudo-fenestral, inter-particle and intra-particle, plant mouldic and interlayer porosity are related to the occurrence of, respectively, the peloidal, coated grain, phyto and dendrite crust travertines. Additionally, dendritic lithotypes have inter-dendrite porosity due to their upward vertical growth and intra-dendrite microporosity.

Organic decay is a first important diagenetic process, and strongly contributes to pore creation. This type of pore creation is evidenced particularly in the formation of plant mouldic porosity (for example, Fig. 4M to T). At facies scale, some other plant related pore types are observed. Plant-framework porosity developed between complex networks of interfingering carbonate coated plant stems. The shelters below plants, which typically bend over on the slopes, lead to considerable macro-porosity. This pore type is of limited importance for the cascade travertines (pores <10 cm), but creates up to 30 m^3 sized primary caves in the waterfall facies. Branch moulds outpacing the lithotype scale are present in the reed and cascade facies.

Dissolution is the second important diagenetic process influencing porosity and appearance of the travertines. For the Faber and Ece travertines, it played a role on a small-scale and resulted in moulds (for example, gastropod moulds; Fig. 17A), and more rounded edges and a vuggy appearance of the mentioned pore types. This is observed particularly below monomictic travertine associated with clayey horizons, for example in the sub-horizontal travertine facies. Petrographic observation of

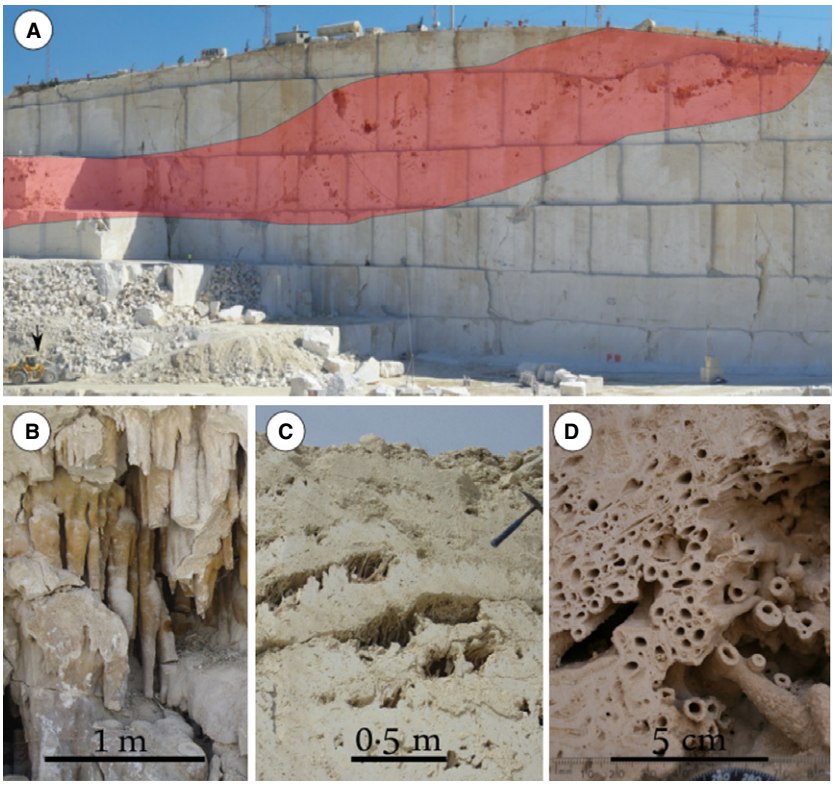

Fig. 9. (A) Distribution of the waterfall facies on the approximate north-east/south-west oriented wall in the Faber quarry, observable from a large distance due to the occurrence of associated cave systems from <1 m³ up to 30 m³ in volume. Bulldozer (see arrow) in the lower left corner for scale. Picture width *ca* 210 m. Total wall height in the middle of the picture is *ca* 50 m. (B) Stalactite-like features hanging from the cave ceiling. (C) Framework (+ shelter) porosity formed by the encrustation of dense plants and their subsequent decay, leading to very porous structures. (D) Combination of mouldic, framework and shelter porosity.

rounded edges and partially dissolved structures (for example, Fig. 17B and C), rims of insoluble residue and selective sparite dissolution (Fig. 17D and E) further manifest dissolution. Sub-crystal moulds (Fig. 17F) and spiky crystals (Folk *et al.*, 1985), as observed by SEM, confirm crystal dissolution (Pentecost, 2005).

Cementation is the third important diagenetic process. The term 'cement' usually refers to mineral precipitates that fill voids or hold the sediment together. In the continental carbonate research field, the term is also applied for a calcite rim coating siliciclastic or biological substrates (e.g. Brasier, 2011). Travertine 'cements' can be formed under the same, or very similar, physico-chemical precipitation conditions as the travertine constituents. In the present study, the term 'cement' is reserved exclusively for secondary, post-depositional features; thus they can be distinguished by the nature of their substrate. Sparites inside a plant mouldic pore, for example, are formed after decay of the plant (for example, Fig. 4Q), and are thus by definition secondary. Consequently, they are classified as cements. Sparites are often observed in the Ece and Faber travertines, usually with an isopachous and euhedral bladed nature of the 50 to 200 μm long sparite crystals (for example, Fig. 4Q). Peloidal micrite fabrics are observed with a similar coating of bladed and dogtooth spars (Fig. 4A to C). Some sparites are partially dissolved. Gastropod moulds are almost completely filled with 50 to 100 μm long, equant cements (Fig. 4AC). Thin-laminated crystalline pendant cements are associated with geopetal silts to fine sands (Fig. 17G). On a macro-scale, the silts and isopachous bladed and micritic cements only slightly reduce porosity.

Along stalactite-like structures, cave linings, fractures and faults, banded cements of varying crystal size sometimes occur (Fig. 17H). These cements vary from micrite and fine-crystalline (<50 μm) blocky crystals to elongated coarse-crystalline sparites; among the latter, radially oriented coarse-crystalline dendrite cements also occur (Fig. 4K and L; El Desouky *et al.*, 2015; Van Noten *et al.*, 2013).

Fabrics typically associated with recrystallization are widespread in the Ballık travertines. Cloudy micrite is found around darker micrite (for example, Fig. 17B and C). The micritic dendrites are surrounded by equidimensional sparites, or are encased by larger crystals. In the latter case the micrites show a sweeping undulose extinction under crossed polars (for example, Fig. 17I). Similar undulose extinction was

Table 2. Overview of the lithofacies of the Ece and Faber travertines.

Depositional system		Depression		Mound	Slope				
FACIES		Sub-horizontal travertine facies	Reed travertine facies		Cascade travertine facies		Waterfall travertine facies		
General description		<5° sloping millimetre to centimetre lamina accentuated by layer parallel porosity	High occurence of plant moulds		1 to 5 cm isopachous continuous lithotype beds. These occur in 10 cm to more than 1 m thick units of one dominant lithotype, or as centimetre-scale cyclic alteranations of two or more lithotypes		Steep slopes >45°. 1 to 5 cm thick lithotype anisopachous and even discontinuous beds. At the dipping point of slopes, plant hash frameworks composed of hollow rods with high interstitial pores. Centimetre large pores to metre-sized caves.		
Sub-facies		/	Biostromal	Biohermal	Smooth slope crenulating sub-facies	Uniformly sloping		Radial phytes waterfall sub-facies	Cave stalactitic waterfall sub-facies	Phyto-boulder waterfall sub-facies
Description sub-facies		/	Metre-scale sub-horizontal bedding but on smaller scale crenulating around plant moulds	Aggradational structures with a high occurence of plant moulds in growth position	Rippling to small terrace layers on slopes of more than 10°	Monoclinal sloping layers on slopes of less than 60°		Alternation of mould-rich and mould-poor lamina on almost vertical slopes.	Centimetre to metre-scale hanging pillar-shaped	Centimetre to decimetre larger phyto-boulders and fingers
Dominant lithotypes		Light and dark peloidal travertine	Phyto travertine, light and dark peloidal travertine		Phyto and dendrite crust travertine and individual micritic dendrites		Phyto and dendrite crust travertines	Phyto and dendrite crust travertines	Phyto lithotypes coated cements including crystalline band travertine	Phyto and dendrite crust travertines
Less dominant lithotypes		Dendrite crust travertine	Thin banded dendrite crusts, Individual dendrites		Peloidal travertines		Peloidal travertine		Inside primary caves: rafts, crystalline bands, crystalline and micritic dendrites	
Minor lithotypes		Matrix-dominated phyto travertines	Allochem travertine between reed moulds		Allochem and monomictic travertines		Allochem and monomictic travertines			
Lithology boundary	Lower contact:	Not observed (quarry bottom)	On top of the sub-horizontal travertine facies and covering the sloping facies (levelling up sequences sensu Guo & Riding, 1998)	Patchy distributed between other facies	On top of the sub-horizontal and reed travertine facies		Always built on the cascade or reed facies.			
	Upper contact:	In the Ece quarry: gradually to reed facies; In the Faber quarry: covered by marl-conglomerate facies	Preceding the onset of the sloping facies and top of the quarry		Precursor of the waterfall facies (increasing slope); covered by reed (decreasing slope)		Always covered by waterfall or reed facies (or non-travertine lithology)			
Size/ dimension		At least ~200 by ~400 m. Minimal thickness of 7 m.	1-20 m thick, lateral extension can be >200 m	Decametre scale in lateral and vertical extension	15 m to more than 30 m thick. Extension over more than 200 by 400 m		Maximum vertical thickness is 15 to 20 m. Horizontal extension >100 m. Isolated geobodies: decametre scale.			
Porosity		Pseudo-fenestral, limited plant mouldic and gastropod mouldic porosity. Porosity is generally low (~5%).	Plant mouldic, fenestral and pseudo-fenestral and gastropod mouldic porosity. Limited interlamina porosity occurs, associated with dendrite crusts. Interparticle porosity occurs related to allochems. Occurence of occasional branch moulds.		Pseudo-fenestral, inter-particle and intra-particle, plant mouldic and interlayer porosity. Plant-framework porosity is formed between complex networks of interfingering overcrusted plants. The shelters below plants, which typically bend over on the slopes, lead to additional macro-porosity. The diameter of the cavernous pores never exceeds 10 cm. Branch moulds occasionally occur.		Due to the occurrence of primary metre-sized caves and the frequent presence of phyto travertines, aditional to the poretypes of the other facies, porosity of the water-fall facies is generally high (>15%).	Highly porous layers with well connected mouldic and small-scale framework porosity. Their alternation with dense micrites and occasionally dendrite crusts reduces connectivity perpendicular to the layering.	The caves can reach up to 30 m^3 in volume but usually are in the order of 1 m^3.	Phyto-boulders have a high mouldic (intra-boulder) porosity. Centimetre to decimetre-large pores between these boulders contribute to the high overall porosity.
Other characteristics/ remarks		Intercalated by mono and polymictic lithologies. High occurence of exposure surfaces and palaeosols. Small bodies are also present intercalated between the reed, cascade and water-fall facies.	Intercalation of cm thick red/brown, semi-consolidated, muddy layers. Exposure surfaces and palaeosols. Affected by weathering at the top of the quarry.		Complex internal structure due to the different flow paths of the down streaming water. Monomictic travertines are associated with concave parts of slopes and their flatter continuation.					
Figure(s):		Fig. 6	Fig. 7		Fig. 8		Fig. 9			

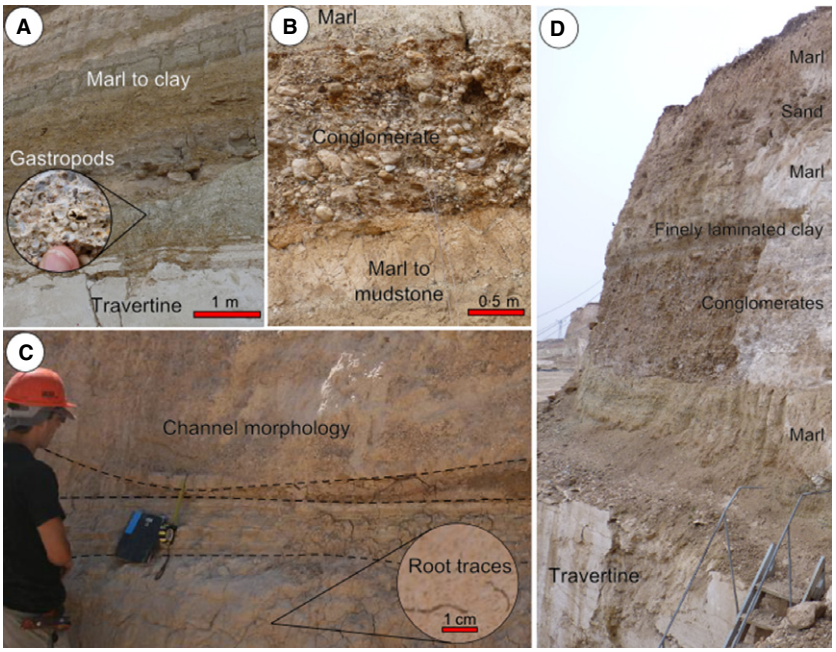

Fig. 10. Characteristics of the marl-conglomerate facies. (A) First marl-conglomerate facies occurrence: varve-like greenish-grey marls with a high gastropod content at the flanks of the Faber quarry. (B) Pebble to cobble-sized conglomerates of the second marl-conglomerate facies occurrence, in the middle of the Faber quarry. Note the imbricated nature of the pebbles, indicative of the palaeocurrent direction. (C) Second marl-conglomerate facies occurrence: channels of conglomerates deposited upon marly units containing root traces. (D) Third occurrence of the marl-conglomerate facies (İlik quarry situated south of the Ece and Faber quarry), overlying the travertines. Top of ladder for scale.

also observed over both peloidal micrite and associated radial sparites.

Acicular crystal morphologies were rarely observed in the Ece and Faber travertines (Fig. 17J); they could result from replacement of aragonite by calcite (e.g. Pentecost, 2005), because the present carbonate mineralogy is only calcite (Khatib *et al.*, 2014). Acicular calcite crystals, however, can occur without an aragonite precursor (Verrecchia & Verrecchia, 1994).

Physical or chemical compaction was not observed. Fracturing of the Faber and Ece travertines did occur and is related to extension in the Denizli and Baklan Basins (Van Noten *et al.*, 2013). Some microfractures of unknown origin were observed (Fig. 17D and E). Sometimes they were subjected to minor dissolution.

Another important process is soil formation. It is associated with geopetal infill, dissolution features, plant roots that can be very similar to reed structures, and gastropods. Manganese-iron oxides/hydroxides colour the travertine from brown to black. However, most palaeosols recognized in the study area yield reworked travertine material in a red-stained matrix. Of importance is that no mature soil profiles have been recognized.

Application of cathodoluminescence (CL) microscopy on the micrite rich, sparite dominant and bladed cemented travertines of the Ece and Faber quarry gives only dull, very dark and dark blue luminescence. With regard to heavily cemented fractures and cements along cave walls, cathodoluminescence allowed observation of an alternation of pink to bright orange-yellow and non-luminescent zones (Fig. 17K and L). For the travertine core of the speleothem-like travertines a very weak luminescence is observed which could be associated with cloudy micrites.

Rubidium–strontium geochemistry

The results of the Rb-Sr trace element and $^{87}Sr/^{86}Sr$ isotope ratio determination are presented in Table 3. The 12 samples analysed display a uniform Sr isotopic signature, independent of the facies in which they occur, with $^{87}Sr/^{86}Sr$ ratios that vary between 0·70785 ± 0·00010 and 0·70792 ± 0·00010, with an average value of 0·70787 ± 0·00010. The samples are characterized by generally high Sr concentrations, varying between 567 p.p.m. and 1839 p.p.m; they also display low Rb concentrations (<0·542 p.p.m.) and very low $^{87}Rb/^{86}Sr$ ratios (<0·002; Table 3). There is no correlation between the $^{87}Rb/^{86}Sr$ and $^{87}Sr/^{86}Sr$ ratios.

Stable isotope geochemistry

The Ece and Faber samples display $\delta^{18}O$ signatures that vary between −9·4‰ and −5·7‰ V–PDB, and $\delta^{13}C$ values between −3·8‰ and +2·6‰ (Appendix S1). The different facies/lithotypes, however, display slight differences

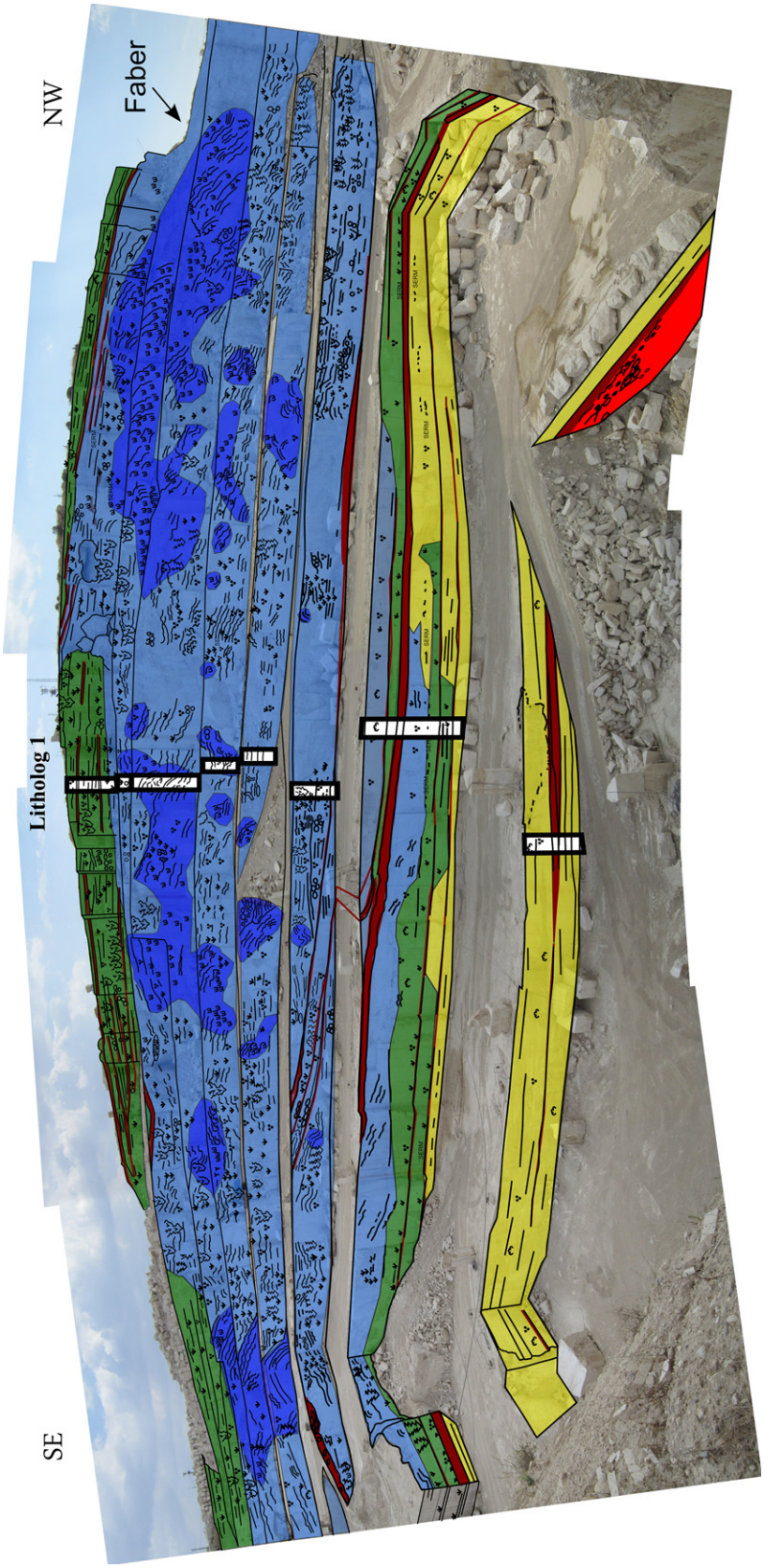

Fig. 11. Illustration of line-drawing of the south-east/north-west wall of the Ece quarry. Width of picture *ca* 360 m. Total wall height *ca* 60 m. The sub-horizontal facies at the base is intercalated by the marl-conglomerate facies. More plants characterize the reed facies and subsequent increasing slopes resulted in cascade and waterfall facies travertines. The sloping system is covered by the sub-horizontal reed facies. Location of stratigraphic section 1 (Fig. 14) is indicated. See Fig. 13 for legend.

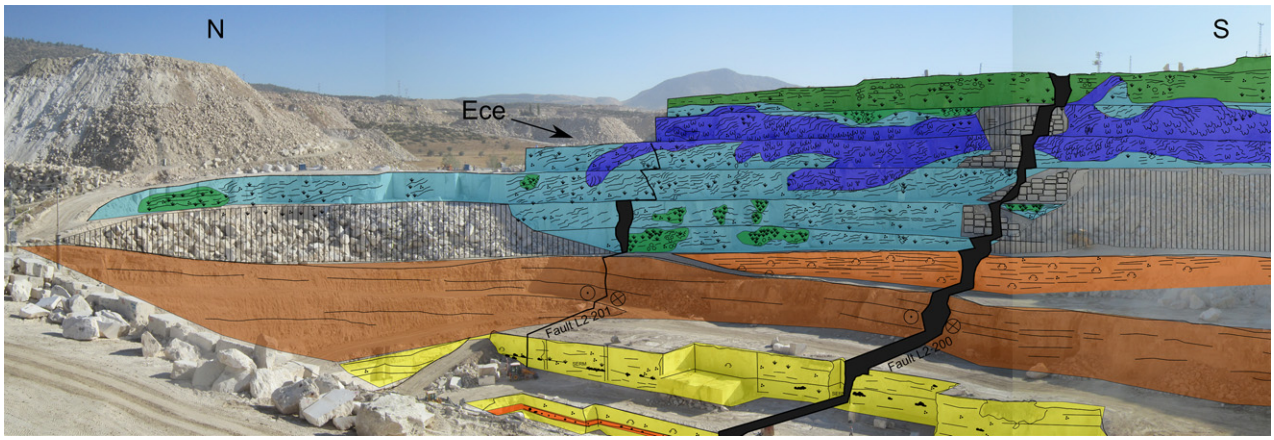

Fig. 12. Line-drawing of the approximate north–south wall of the Faber quarry. Width of picture *ca* 300 m. Cumulative wall height 60 to 70 m. The sub-horizontal facies that is intercalated by polymictic travertines, is cut-off by the marl-conglomerate facies. Travertine precipitation with time transitionally regained domination within the system. The smooth-sloping cascade travertines evolve into steeper waterfall systems that are covered by the sub-horizontal reed facies. See Fig. 13 for legend. Faults L2.200 and L2.201 (Van Noten *et al.*, 2013) are indicated.

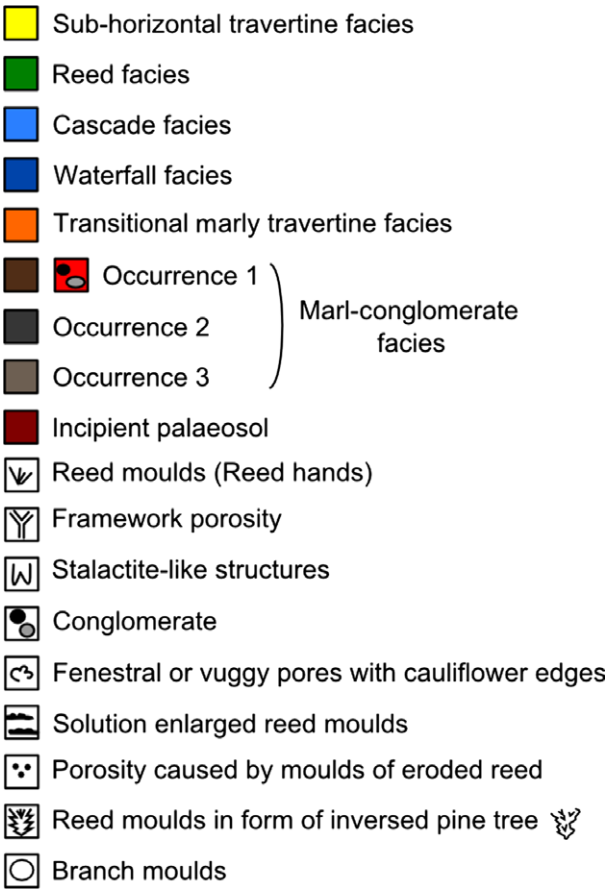

Fig. 13. Legend for Figs 11, 12, 15 and 16.

(Appendix S1, Fig. 18A). Travertines from the sub-horizontal facies are on average the least depleted, both in $\delta^{18}O$ (−6·9‰ V-PDB) and in $\delta^{13}C$ (+1·0‰ V-PDB). The cascade facies exhibits lower values than the sub-horizontal facies (average $\delta^{18}O = -7{\cdot}6‰$ V-PDB and $\delta^{13}C = +0{\cdot}3‰$ V-PDB), but not as negative as the waterfall facies (average $\delta^{18}O = -7{\cdot}9‰$ V-PDB and $\delta^{13}C = -0{\cdot}1‰$ V-PDB). The reed facies finally is characterized by the lowest $\delta^{13}C$ values (on average −0·6‰ V-PDB). The average $\delta^{18}O$ value of the reed facies (−7·3‰ V-PDB) is lower than that of the sub-horizontal facies, and clusters together with those of the cascade and waterfall facies. Peloidal travertine is generally enriched in ^{13}C, and phyto travertines show relatively low $\delta^{18}O$ values. The high variability in $\delta^{18}O$ and $\delta^{13}C$ values of the polymictic travertines, marls and conglomerates can be explained by their heterogeneous nature. This is particularly pronounced for one sample with extreme values both for $\delta^{18}O$ (−9·4‰ V-PDB) and $\delta^{13}C$ (−3·8‰ V-PDB). Other samples also show signatures that deviate from the overall facies clusters (Fig. 18A).

The variation in $\delta^{18}O$ and $\delta^{13}C$ signature was plotted along the stratigraphic sections. In Fig. 18B, an example is given for the stratigraphic section of Ece described in Fig. 14. No first order correlation between $\delta^{18}O$ and $\delta^{13}C$ was observed. While $\delta^{18}O$ stays relatively constant over the entire section, a first order continuous decrease of $\delta^{13}C$ can be observed towards the top of the quarries. The stable isotope oxygen and carbon signatures of the Faber quarry samples are similar to those of samples collected from the Ece quarry.

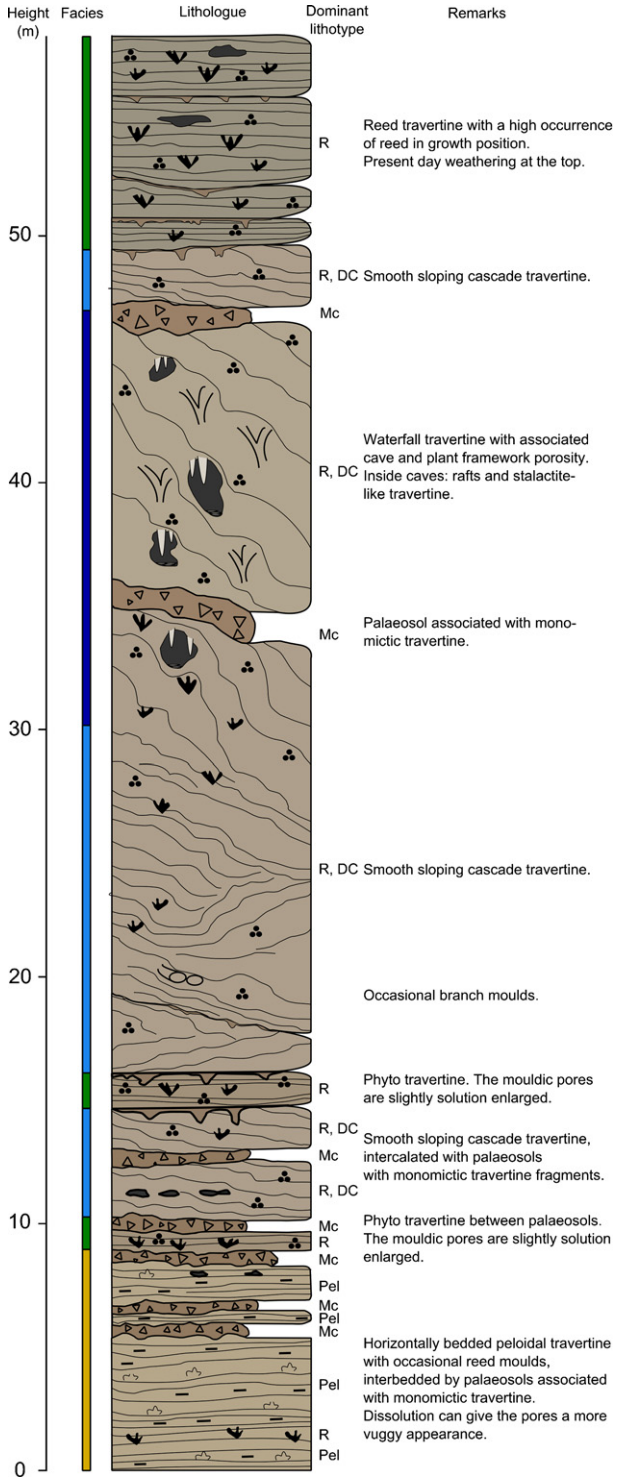

Fig. 14. Stratigraphic section 1 of the Ece quarry. Evolution from the sub-horizontal facies (yellow) at the bottom towards the reed facies (green) and cascade facies (light blue), intercalated and cut-off by erosional surfaces and/or palaeosols. A temporal reed facies is again cut-off before the system evolves into the cascade facies, and with increasing slope to the waterfall facies (dark blue). When the slope diminishes the smoother sloping cascades take over again, before being covered by the reed facies. (Pel, peloidal micrite travertine; R, phyto travertine; Mc, monomictic travertine; DC, dendrite crust travertine).

DISCUSSION

Depositional setting of lithofacies

In the following paragraphs the different lithotypes and lithofacies will be interpreted in order to reconstruct the depositional environment and its evolution through time. The discussion will first address the dominantly sub-aqueous deposits (i.e. sub-horizontal and biostromal reed travertine facies) that are followed by a period of subaerial exposure as manifested by the erosional surface in the Ece quarry that grades laterally into marl-conglomerates. Subsequently the dominantly sub-aerial deposits and their vertical stacking will be addressed. Finally the uppermost travertine and non-travertine strata will be discussed.

The dominantly sub-aqueous deposits

The lack of any significant inclination of the sub-horizontal travertine facies and the comparison with active analogues (for example, Pamukkale; Fig. 1) supports travertine formation in depressions with periodic short-term exposures causing moderate erosion of previously precipitated travertine. The observations are in agreement with the environmental interpretation of shallow lakes fed by hydrothermal vents (Özkul *et al.*, 2013). Observed lithotype cross-cutting relationships imply physical erosion during drops or even periodic interruption of carbonate precipitation due to discontinuous water flow or changes in flow path, as indicated by erosional surfaces. The monomictic travertine layers, associated with clayey horizons, with dissolution enlarged pores beneath these layers, and their reddish colour, can all be interpreted as being the result of incipient soil formation and/or meteoric oxygen-rich water infiltration. Mature soils, which would indicate prolonged periods of exposure and thus correspond to strongly reduced precipitation rates, however, have not been recognized. The red to brown and black colours in the soils relate to iron and manganese oxidation, reflecting changing redox conditions. The sub-hori-

zontal travertine facies largely corresponds to the marsh-pool facies of Guo & Riding (1998) and shows similarities to the lacustrine and paludal facies of Ford & Pedley (1996) and the shallow lake fill deposits of Chafetz & Folk (1984).

The main difference between the subsequent biostromal reed facies and the sub-horizontal travertine facies is the high occurrence of plant moulds. In order for plants to grow, the environment should not be too harsh and the water should not be too deep or too hot. Some bryo-

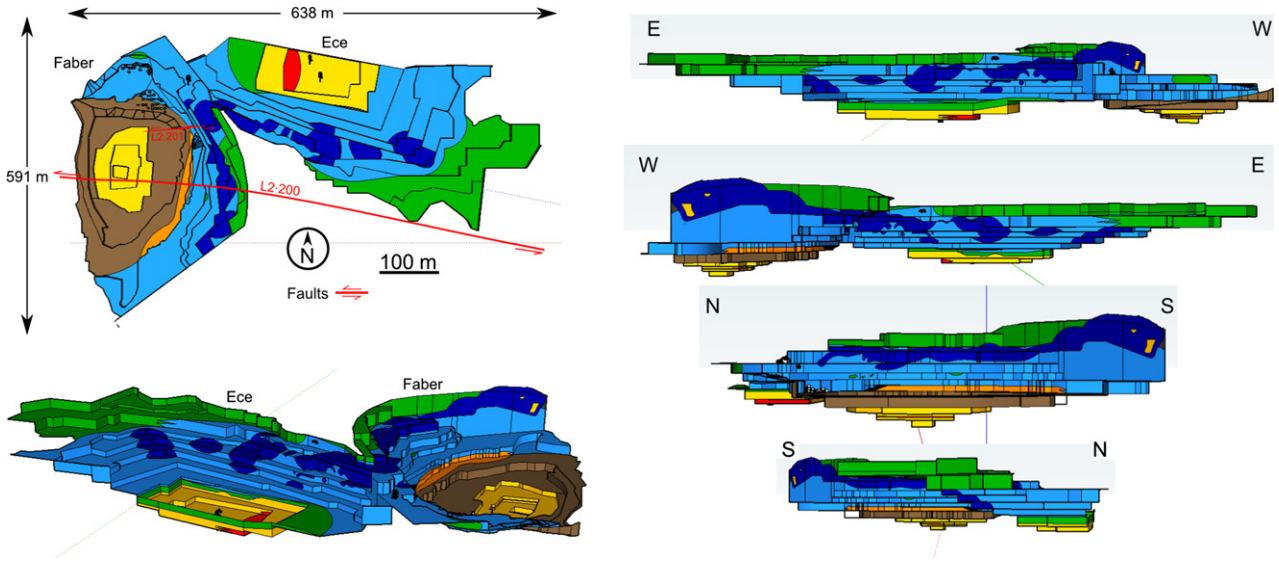

Fig. 15. Lithofacies distribution in the Ece and Faber quarries based on the projected detailed line drawing on the quarry walls. See Fig. 13 for legend. Faults L2.200 and L2.201 (Van Noten *et al.*, 2013) are indicated. Maximal cumulative wall heights of the Ece and Faber quarry are 61·4 m and 90·2 m, respectively (without covering non-travertine facies).

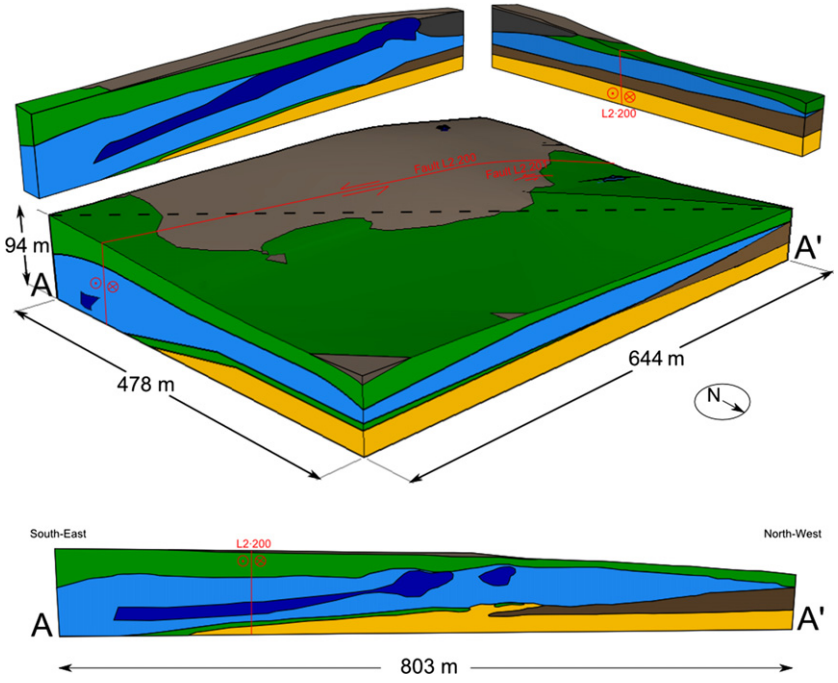

Fig. 16. Extrapolated 3D lithofacies distribution inside and outside the quarries. Illustration of different sections taken through the model. See Fig. 13 for legend. Faults L2.200 and L2.201 (Van Noten *et al.*, 2013) are indicated.

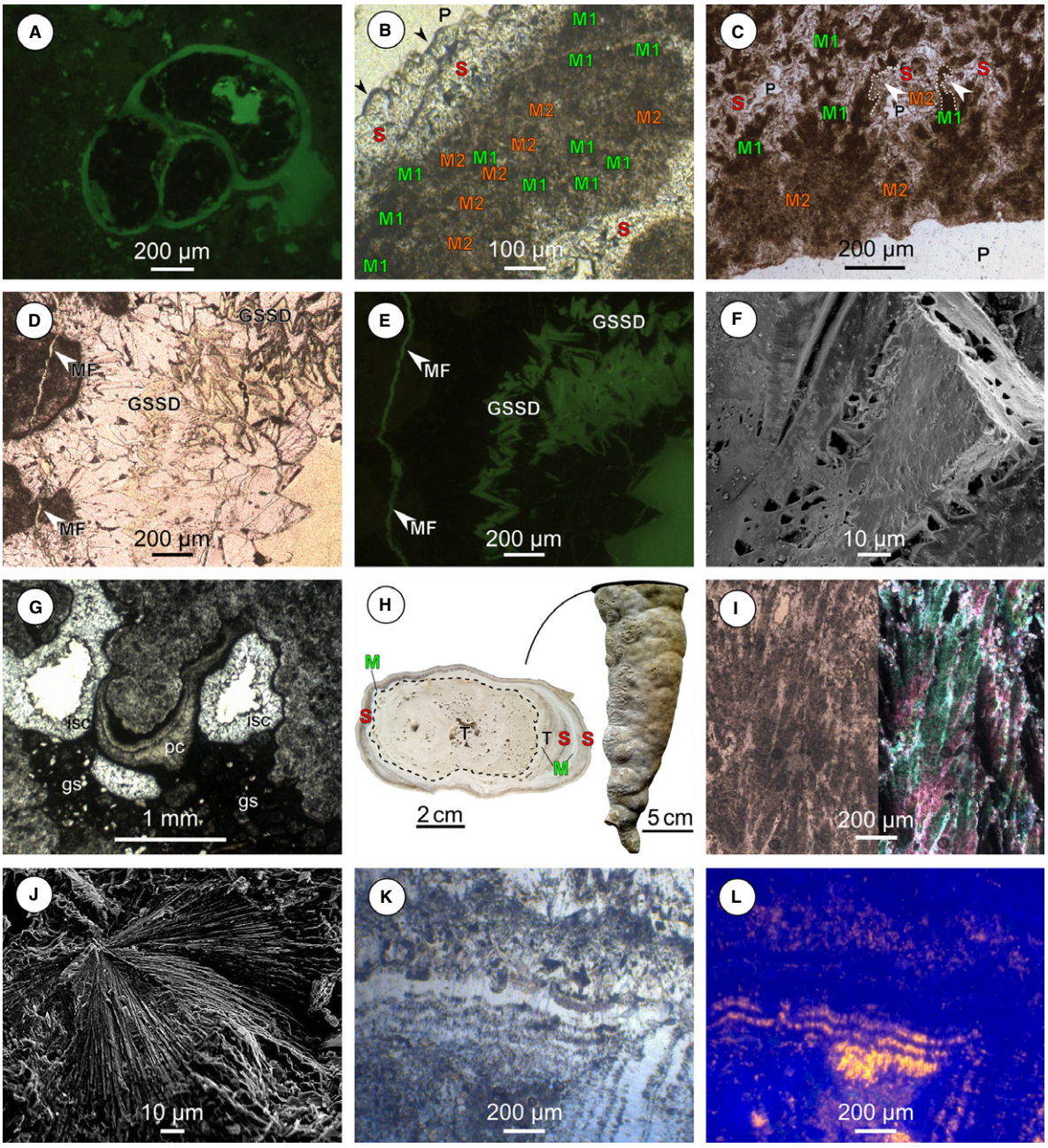

Fig. 17. Diagenesis features in the Ballık travertines. (M1, primary micrite; M2, secondary micrite; M, micrite; S, sparite; P, porosity; MF, micro-fracture; GSSD, generation specific sparite dissolution; pc, pendant cements; gs, geopetal silts/sands; isc, isopachous sparite cements; T, travertine) (A) Photomicrograph of gastropod mould under fluorescent light. (B) Photomicrograph illustrating the darker primary and secondary cloudy micrite. Sparite crystal edges have been subject to dissolution. (C) Photomicrograph illustrating dissolution (white arrows) of primary micritic dendrites. The cloudy micrite (M2) is the result of micritization. (D) Photomicrograph showing an example of microfracturing and generation selective sparite dissolution. (E) Photomicrograph under fluorescent light showing an example of microfracturing and generation of selective sparite dissolution. (F) SEM image with sub-crystal moulds. (G) Transmitted light photomicrograph with pendant thin-laminated crystalline cements associated with geopetal silts to sands, followed by isopachous sparite cements. (H) Photograph of stalactite-like structure with a travertine core surrounded by micrite and sparite cementation. (I) Photomicrograph under parallel (left) and crossed polars (right) of micritic dendrites illustrating their undulous extinction under crossed polars, suggesting recrystallization. (J) SEM image of needle morphologies (K) Optical photomicrograph of fracture cements. (L) Enhanced (saturation increased) cathodoluminescence photomicrograph of the fracture cements in (K) with dark blue, dull pink and bright yellow-orange luminescence.

Table 3. Results for Rb-Sr trace element and $^{87}Sr/^{86}Sr$ isotope ratio determination for 12 samples from the Ece and Faber quarries (2σ for Rb <0·0084 p.p.m.; for Sr <9·3 p.p.m.; for $^{87}Rb/^{86}Sr$ <0·00003; for $^{87}Sr/^{86}Sr$ <0·00011).

Quarry	Sample	Facies	Rb (p.p.m.)	Sr (p.p.m.)	$^{87}Rb/^{86}Sr$	$^{87}Sr/^{86}Sr$
Ece	EC10HC001	Sub-horizontal	0·041	864·4	0·00014	0·70785
	EC10HC006	Sub-horizontal	0·249	663·4	0·00109	0·70785
	EC10HC021	Waterfall	0·064	728·1	0·00026	0·70788
	EC10HC031	Sub-horizontal	0·126	742·0	0·00049	0·70787
	EC10HC036	Cascade	0·020	1838·9	0·00003	0·70785
	EC10HC048	Cascade	0·283	726·5	0·00113	0·70788
Faber	FA10JS001	Cascade	0·068	593·1	0·00033	0·70788
	FA10JS008	Waterfall	0·026	620·4	0·00012	0·70788
	FA10JS020	Reed	0·542	1048·9	0·00150	0·70792
	FA10JS022	Sub-horizontal	0·185	608·8	0·00088	0·70787
	FA10JS035	Marl-conglomerate	0·376	567·2	0·00192	0·70787
	FA10JS053	Cascade	0·157	898·7	0·00051	0·70786

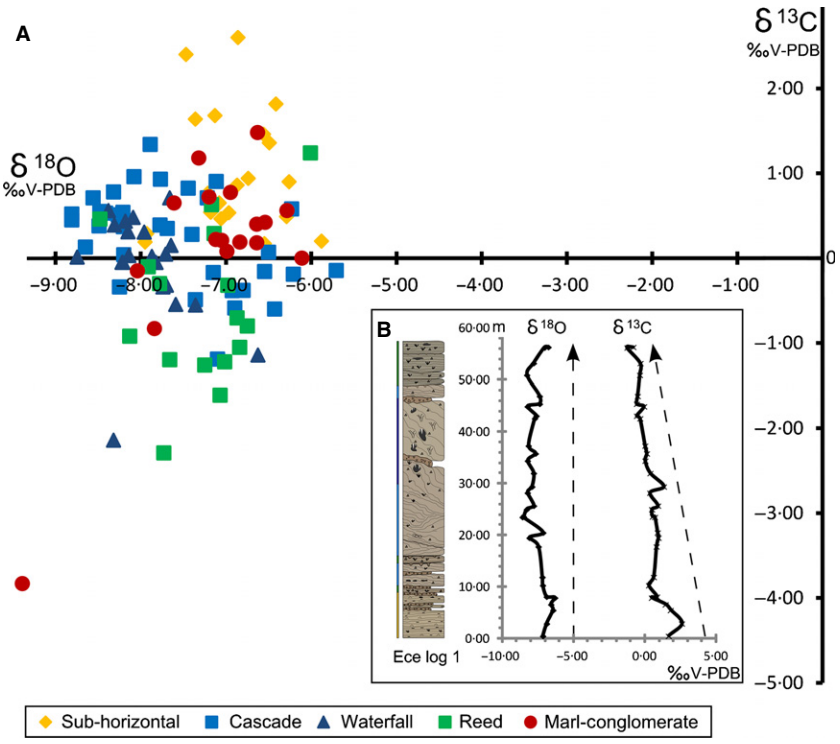

Fig. 18. (A) $\delta^{18}O$–$\delta^{13}C$ cross-plot of samples from different facies (data: Appendix S1). (B) $\delta^{18}O$ and $\delta^{13}C$ values plotted vertically along the first stratigraphic section of Ece (Fig. 14). Note the decrease in $\delta^{13}C$ values from bottom to top.

phytes are reported not to tolerate temperatures higher than 20°C (Glime & Vitt, 1984). Bryophytes can thus be considered as good environmental indicators. However, not all plants were necessarily alive during encrustation. When reed stems are eroded, for example, they can be transported from their original setting, recognizable by their sub-horizontal arrangement; their presence therefore might not always represent the temperatures of the facies in which they are found. Plants clearly acted as a substrate for travertine precipitation and as sediment trappers. These processes promoted the vertical outgrowth and led to the creation of some minor topography. The plant moulds are often associated with the centimetre-thick red/brown, unconsolidated, muddy layers, which could be interpreted as the onset of soil formation or a phase with a relatively high siliciclastic contribution.

The 'reed mound facies' of Guo & Riding (1998) and the 'spring mound facies' of Janssen

(2000) are inherently linked with a mound geomorphological development. In the travertines studied here, the mound morphology of individual facies is not apparent in the biostromal reed travertines and the existence/location of springs is unclear. Consequently, on a facies scale it can be argued that the reed travertine facies defined here partly coincides with the reed mound facies and to a sub-facies of the marsh-pool facies of Guo & Riding (1998). Therefore, for the biostromal reed travertines, a setting with small ponds and small rivers and temporarily and/or locally incipient soil formation is inferred. There is a combination of *in situ* reed growth and transported reed accumulation.

The marl-conglomerate intercalation

The lowermost occurrence of the marl-conglomerate facies cuts into the previous facies. It is marl dominated but contains a large conglomerate fraction. The marls illustrate the input of two different types of sediment, namely an external siliciclastic and a proximal travertine system. The dominantly fine-grained nature of these sediments is indicative of a shallow and low energy environment. Although no varves were observed, a lacustrine or palustrine environment seems the most plausible. The locally observed root traces support the shallow nature of these deposits, with temporary plant growth. However, no reed traces were recognized.

Within the marls, lenticular shaped conglomerate bodies occur. Based on the decimetre-scale channel erosive base of the marl-conglomerates, organized pebbles with an imbricated nature and the existence of interpebble porosity, a fluviatile origin is suggested, an interpretation in line with the conclusions of Khatib *et al.* (2014). The rounded pebbles indicate that they result from a long distance transport or from reworking of a rounded pebble deposit nearby. The composition of the pebbles and other detrital material reflects the lithology and mineralogy of adjacent geological formations (Khatib *et al.*, 2014), and the travertine pebbles reflect erosion of nearby travertines. The size of the pebbles indicates strong palaeocurrents which, based on the imbrications, reflect a WNW direction.

Based on the projection of the slope of the top and bottom of the facies in the Faber quarry, this facies would be 1 m thick in the Ece quarry where it would occur just above the deepest quarry level. The observed polymictic travertine to conglomerate in the west of the Ece quarry, which changes into an erosional surface more to the east, is therefore interpreted as the lateral equivalent of the marl-conglomerate facies in Faber. This marl-conglomerate thus reflects a non-travertine-dominated and dominantly lacustrine–palustrine depositional system in which the presence of river deposits testifies to short high hydraulic energy events bringing in large pebbles from the hinterland and locally eroding travertines.

The sub-aerial (thin water film) deposits and their lateral equivalents

The previous facies are followed by the cascade facies. In order for the sloping facies to form, a significant topography is necessary. This can occur when travertine precipitation takes place on a topographic relief (such as in the present-day Pamukkale setting) or when topography is self-generated by travertine development. The latter can develop due to a higher precipitation rate proximal to the springs/vents caused by the decreasing supersaturation along the flow path. An additional possibility is the encrustation of both eroded plants and plants in growth position. Plants not only act as precipitation substrates, but also as sediment traps, as previously described for the reed facies. The subsequent encrustation results in a crenulating nature of the laminae and the solidification of small topographic elevations. The irregularities cause increases in turbulence, with related increases in degassing, thus enhancing precipitation. Once topography has formed, down-flowing water leads to precipitation of the different cascade travertine lithotypes. Crusts are suggested to form from fast-flowing water by rapid precipitation (Guo & Riding, 1998; Chafetz & Guidry, 1999; Barilaro *et al.*, 2012), with the thickness of the laminae corresponding to the minimal thickness of the water film. The phyto lithotypes resulting from eroded plants and coated grain travertines indicate a high energy environment. Monomictic fragments in a brown-red clayey matrix, that locally occur, result from reworked travertine in relation to a spatial or a temporal precipitation stop. The encrustation of patchy distributed plants results in build-ups of biohermal reed travertine (Fig. 12).

Comparing to literature, the biohermal reed facies does coincide with the 'reed mound facies' of Guo & Riding (1998) and the 'spring mound facies' of Janssen (2000). The cascade facies includes the terrace slope facies and the

smooth slope facies of Guo & Riding (1998) and the sloping mounds and terraced mounds of Chafetz & Folk (1984). The widespread occurrence of the sloping facies indicates the formation of a central elevated topography. This could be related to a large fissure ridge or even a set of fissure ridges. So far, however, these have not been observed.

The waterfall facies can be interpreted as the result of slopes that became too steep (>45°) to precipitate isopachous continuous layers and is regularly induced by plants overhanging rims. The caves (and smaller equivalent pores) are interpreted as primary syn-depositional features that formed by precipitation on overhanging plants sheltering the caves on the dipping point of slopes. The structures are comparable to the bryophyte curtains described in Pedley *et al.* (2003). The caves should not be mistaken for karstic features. The plants themselves became encrusted and after decay led to small-scale mouldic porosity in addition to framework porosity. When plants tend to hang down over or inside the sheltered spaces, their encrustation and subsequent cementation will give rise to the development of stalactite-like structures. Similar processes were observed in active travertine systems, for example in Pamukkale (Fig. 19C). Rafts are formed by carbonate precipitation in static waters inside the caves. The rafts indicate that the caves temporarily were only partially filled with water. Rafts can break and settle due to their increasing weight caused by continuous precipitation or due to a decrease of water volume below the rafts that supported the structures. After settling, they can become covered by cements, giving rise to structures in which several rafts are cemented together. The raft setting contrasts with the phreatic conditions that are necessary to precipitate the observed cave cements that fringe the cave walls.

The dendrites in the caves probably formed in small, rather static pools. The sheltering plants and subsequent travertine precipitation could have limited the light incidence, thus restricting photosynthesis, making it impossible for higher plants or organisms to thrive. This would be in agreement with the 'harsh' environments as described by Chafetz & Folk (1984), where microbes will have a larger influence on the fabric formation.

The described waterfall facies of Ece and Faber resemble the waterfall deposits of Golubic (1969) and Chafetz & Folk (1984) and could be equivalent to parts of the Plitvice waterfalls in Croatia (Chafetz *et al.*, 1994) or the Güney Waterfall in Denizli, Turkey (Özkul *et al.*, 2010). Lateral to the waterfall, cascade and reed biohermal travertines, marl and/or marl-conglomerates are observed. The latter correspond with the

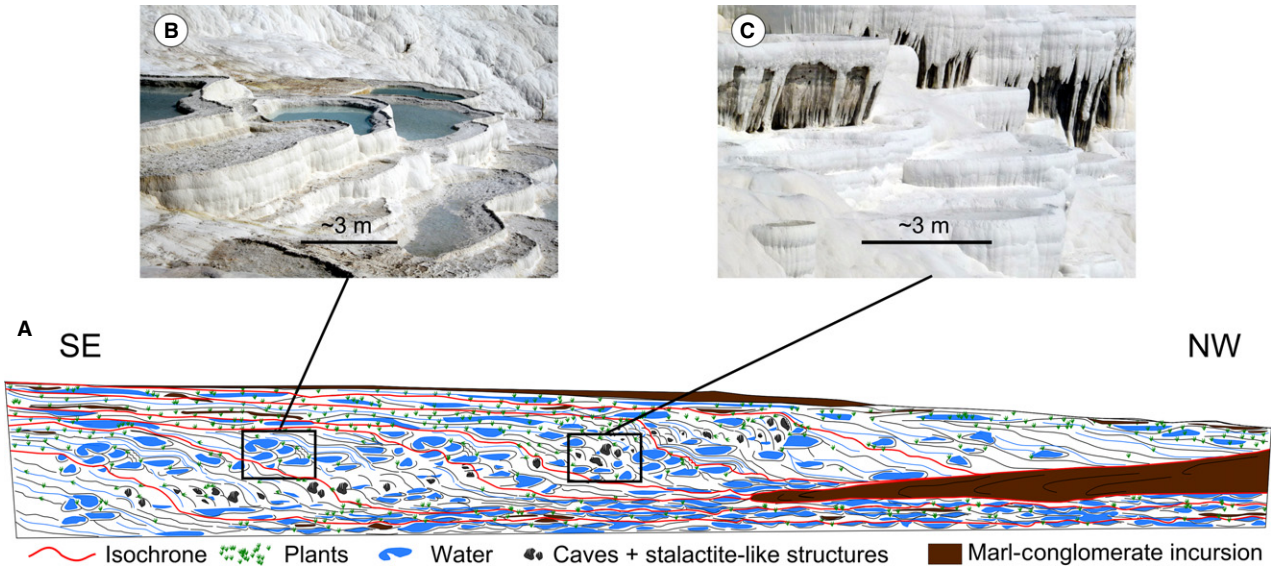

Fig. 19. (A) Interpretational drawing of the depositional environment along the A–A' transect in Fig. 16. Note the stacked prograding trend of the travertine deposits. (B) Possible actual analogue of the cascade travertine facies in the present-day Pamukkale travertine outcrop. (C) Speleothem-like structures of the waterfall travertine facies in the present-day Pamukkale travertine outcrop.

greenish grey, cream-coloured lake-marsh deposits described by Özkul *et al.* (2002) and reflect an adjacent lacustrine environment where there is a dominant influx of detrital material. Periodically some rivers imported coarser material into these lakes.

The uppermost travertine and overlying non-travertine strata

Biostromal travertines, similar to those encountered in the lower part of the quarries but with a higher occurrence of erosional surfaces, cover the previous facies, reflecting a small pond to palustrine environment. Towards the top, the change in travertine colour reflects a higher contribution of non-carbonate constituents, before finally marls with coarse grained sands, showing one-directional low-angle cross-bedding and conglomerate intercalations, typical for an alluvial depositional system, mark the end of travertine deposition.

Large-scale geobody architecture

The 3D visualization of the lithofacies (Figs 10 to 15) requires and stimulates consideration and discussion of the thickness and lateral variations of the facies. The large-scale depositional travertine system can best be compared to the mound/fissure ridge complex development as described by Pentecost (2005), with the spring locations controlled by the tectonic activity within the Denizli Basin (Van Noten *et al.*, 2013). However, the exact position of the main fluid vent was not found inside or near the quarries. Based on the north-west-dipping slopes of the deposits, the main source should be located south-east of the studied quarries, near the centre of the domal area. The lateral extension of the sub-horizontal travertine facies suggests at least one additional major source at the time of travertine precipitation.

In contrast with the travertine depositional models of Pentecost (2005), the Ballık system developed on a much larger scale and additionally included steep cascades, waterfall systems and distal sub-horizontal travertines deposited in shallow pools. Based on the deduced depositional environments of the lithofacies and their lithotypes a conceptual depositional model can be developed (Fig. 19).

The travertine build-up can be split up into four main systems. The first system, represented by the sub-horizontal and biostromal reed travertines, formed in a shallow dominantly sub-aquatic environment. The second system consists of the non-travertine intercalation while the third system consists again of travertine, mainly represented by the sloping facies, formed in a thin water film in a dominantly sub-aerial setting. The boundary between the two travertine systems is particularly pronounced in the Faber quarry in the form of the marl-conglomeratic incursion that laterally evolved into an erosional surface in the Ece quarry. Finally the fourth system reflects the levelling up of the travertine system with a gradual transition to dominantly marly lacustrine strata.

The sub-horizontal facies show aggradational stacking patterns. A general progradation of travertine development is apparent based on the occurrence of stacked waterfall travertines. The progradation results in sigmoidal clinoforms with downlap terminations, mainly against the laterally occurring marl-conglomerate deposits.

The Ballık travertine dome is estimated to be *ca* 100 m high (for example, Fig. 16). The size and morphology, as well as the extensional tectonic setting, are in good accordance with the aggradational carbonate build-ups reported for the Pre-Salt of the Atlantic (Buckley *et al.*, 2013). Furthermore, Sharp *et al.* (2013) described fissure ridge and 'dam and cascade' travertines related to extensional–transtensional faults for the onshore Pre-Salt equivalent in the Namibe Basin (Angola). The here presented lithofacies geobody model in combination with petrophysical, including porosity and permeability, and acoustic data (Soete *et al.*, 2015) can thus form a possible basis for a reservoir analogue and synthetic seismic modelling of the Pre-Salt carbonates and other domal travertine reservoirs worldwide.

Diagenesis

Early diagenetic processes, such as organic matter and plant decay, must have been omnipresent in the Ece and Faber travertines. Cloudy micrite at least partly evidences a diagenetic (micritization) origin (Fig. 17B and C) and undulose extinction over micrite (for example, Fig. 17I) and over both micrite and sparites points towards recrystallization. At the microscale, dissolution and recrystallization, including micritization and sparitization, are thus clearly visible (Fig. 17). For some fabrics, distinction between primary and secondary fabrics remains a problem, particularly for sparites. This problem is discussed in more detail by, for example, Brasier *et al.* (2011). Large-scale diage-

netic overprinting was limited, because no major karstification occurred and considerable cementation is restricted to fractures, faults and primary cave systems. The open pore system of the travertines has probably led to a high initial water–rock interaction and an associated fast saturation for infiltrating waters. On the scale of the whole mound, this implies contact with relatively buffered fluids, thus limiting additional water–rock interaction.

Kallis *et al.* (2000), Mallick & Frank (2002), Sant'Anna *et al.* (2004) and Sierralta *et al.* (2010) reported, in accordance with the present study, a generally low luminescence for continental carbonates. The observed 'dull blue' emission, also referred to as 'background blue', was recognized in the Heidenheim-Mergelstetten freshwater carbonates (south-west Germany) by Kallis *et al.* (2000). It occurs only in calcite with low iron contents (Richter & Zinkernagel, 1981) or in calcite that contains no activators or quenchers (Amieux *et al.*, 1989). Machel *et al.* (1991) suggested a type of lattice defect to be responsible for the non-luminescent background blue. Based on these cathodoluminescence properties, Kallis *et al.* (2000) suggested a vadose diagenetic cementation, where the oxidative conditions prohibit the incorporation of Mn^{2+}, the main activator, in the travertines (Machel, 2000). The pendant thin-laminated crystalline cements and geopetal silts and sands that are observed in the Ece and Faber travertines, are consistent with a vadose environment.

Based on the weak pink-orange and bright orange-yellow luminescence along fractures and in the travertine cores of the speleothem-like structures, a steadily higher Mn^{2+} content (Machel *et al.*, 1991), and relatively low quencher content (Machel, 2000) is deduced. For the travertine cores of speleothem-like structures, the cements could lead to locally reducing conditions. The zones associated with organic-rich micrites were the most prone to recrystallization, explaining their preferential weak luminescence. The isopachous cements of the speleothem-like structures are also found coating the cave walls and thus reflect phreatic conditions (El Desouky *et al.*, 2015). The isopachous and euhedral bladed nature of the sparite crystals that surround the micrite matrix of the travertine samples is also consistent with a phreatic realm. For the cemented fractures, luminescence also seems related to the presence of organic matter, and a similar interpretation is therefore suggested. These fabrics thus reflect alternating vadose and phreatic meteoric conditions, illustrated in Fig. 17G, in which vadose pendant cements and silts are followed by isopachous phreatic sparite cements.

Microbial influence on travertine fabrics

Dendrite crusts

Deducing whether precipitation was biotic or not is challenging based on fossil deposit observations. Environmental SEM observations show that the Ballık micritic dendrites are characterized by up to 100 μm sized tubular pores that are associated with honeycomb and bacteriform structures, as well as encrusted bacterial or fungal filaments (Fig. 5C to F). Processes such as dissolution, however, can result in micron-sized spheres with shapes similar to bacteria and formation of tubes could be related to (abiotic) crystal growth (for example, the dendrite crystals of Jones *et al.*, 2000). However, the fact that these structures occur together points to a biotic influence. Moreover, the dark organic-rich micrite follows the bush morphology (for example, Fig. 4E to G and Q) revealing a depositional relation, and probably a depositional origin. Similar dendrites with epifluorescent organic matter were also observed by Chafetz (2013), who attributed the microporosity (Figs 4G and 5C to F) to microbial decay. Furthermore, the observed fabrics (Fig. 5C to H) strongly resemble fabrics that formed around bacterial clumps and cyanophytes as described by Casanova *et al.* (1999), the bacteriform bodies and fungal or bacterial filaments of Guo & Riding (1994), and/or the *Phormidium* filaments of Golubic *et al.* (2008) that diagenetically altered into palisade crystals. Défarge *et al.* (1996) showed similar alveoli with walls made of polysaccharide fibres derived from sheaths of dead cyanobacteria. A microbial substrate, and nucleation mediation, thus seems highly likely for the dendrite crusts, that also are observed around plant moulds in the phyto lithotypes.

In a continental carbonate context, the term 'shrub' is reserved for: "morphological shrub-like, fern-like or bush-like arborescent growths that branch upward to form colonies, resembling miniature forests" (Chafetz & Folk, 1984). The Ballık micritic dendrites can thus be regarded as shrubs. Chafetz & Guidry (1999) distinguished three bacterially induced kinds of shrubs, namely ray-crystal, crystal and bacterial shrubs reflecting an increasing relative contribution of bacterially induced precipitation in comparison

to abiotic mineral precipitation. The Ballık micritic dendrites and crystalline dendrites are considered equivalent to the bacterial and crystal shrubs, respectively. The micrite dendrite crusts show many macroscopic similarities to the crystalline crust travertine or feather crystal crusts that, according to Guo & Riding (1998), consist of elongate calcite crystals, the so called 'ray crystals' (Chafetz & Folk, 1984; Folk *et al.*, 1985), 'calcite feather crystals' (Guo & Riding, 1992) or 'dendritic calcite crystals' (Jones & Kahle, 1986). However, a major discussion point is the crystallinity of these features. Although Guo & Riding (1998) mentioned that in thin-section the 'crystalline' crusts are often micritized, a dendritic micrite fabric was not described. The presence of dendritic organic rich micrite in the Ece and Faber samples is high and probably has a partial depositional origin. The Ece and Faber dendrite crusts thus are more likely to represent different stages in the diagenetic sequence to travertine laminated crusts, as suggested by Love & Chafetz (1988), with the main acting process being post-depositional crystal growth, as pointed out by Brasier *et al.* (2011). The initial diagenetic stages were also illustrated by Janssen *et al.* (1999). The observed sweeping undulose extinction of the dendrites enforces this hypothesis. Subsequent cloudy micrite formation around organic rich micrite was observed, equivalent to the sparmicritization described by Guo & Riding (1994).

Peloidal travertine

The peloidal lithotypes are one of the dominant lithotypes for the Ece and Faber travertines in agreement with Folk & Chafetz (1983) and Chafetz & Folk (1984), who describe clumps as the elementary building blocks for travertines throughout central Italy and the west-central USA. Riding (2000) described peloidal micrite as the main microfabric of microbial carbonates, resulting from calcification of bacterial cells, sheaths and biofilm, and from phytoplankton-stimulated whiting nucleation. Peloidal fabrics, however, can also be allochthonous when they result from micro detrital processes (Ford & Pedley, 1996). A detrital allochthonous origin seems less likely than *in situ* microbial formation as pseudofenestral porosity would have been eliminated in the case of a detrital origin and because no traction structures were observed. In the particular case of detrital particles trapped on sticky microbial clots, however, the fabrics could show similar properties. The observed transitional nature towards the micritic bush fabrics also suggests microbial involvement.

Fabric formation processes

Based on detailed petrographic and SEM observations and literature comparison (e.g. Guo & Riding, 1994; Dupraz *et al.*, 2004; Turner & Jones, 2005; Rogerson *et al.*, 2008), it is postulated here that mucus/extracellular polymeric substances (EPS) around microbial colonies, and in particular their filaments, provided suitable environmental conditions and acted as nucleation sites in supersaturated waters and thus became calcite coated. Depending on the conditions, the crystal size of the coatings will vary, where micrite will form more easily or could well be nucleated in the biofilm (Guo & Riding, 1994). Growth of the microbes on a substrate mediates $CaCO_3$-precipitation resulting in dendritic fabrics (including micritic peloidal dendrites), whereas precipitation in the water column resulted in the formation of individual peloids. Decay of the microbial matter probably initiated rapidly after coating and could even be contemporary for different closely spaced locations. The gradual decay of these organic structures results in acids that will dissolve the calcite creating organic-rich micrite associated with micro-mouldic porosity (for example, Figs 4F, 4G and 5C to F), as described by Chafetz & Folk (1984). Subsequently, dominantly physico-chemical precipitation takes over, and leads to sparite formation around the micritic clumps (Fig. 5C). From here on, fabric formation is dominantly abiotically controlled, similar to the sparry crusts reported by Janssen *et al.* (1999) that formed due to cementation and recrystallization of cyanobacterial micritic bushes. Micritic peloidal dendrites recrystallize to straighter, elongated, semi-crystalline micritic dendrites with an undulose extinction of the dendrites. Post-depositional crystal growth will gradually obscure the original microbial signature and crystal size will increase with time. Micritization (Guo & Riding, 1994) occurs mainly in relation to the decay of organic matter. For the phyto travertine lithotypes a similar formation mechanism is envisaged, during which plant structures acted as substrates for mucus and subsequent travertine precipitation. The decay of plant structures, as for the microbes, starts very shortly after their coating that inhibits further plant growth.

Geochemistry

Strontium isotopes

McArthur & Howarth (2004) stated that a correction for the *in situ* decay of ^{87}Rb might be required when Rb concentrations exceed 0·1 p.p.m., which is the case for some samples. However, even for an age of 1·78 Ma, i.e. the oldest travertine precipitation age reported for the Ballık travertines (Lebatard *et al.*, 2014), corrections result in insignificant changes. The Sr isotopic signatures of the travertines thus directly reflect the isotopic composition of their precipitating fluids (El Desouky *et al.*, 2015). The uniform Sr isotope ratios (0·70785 to 0·70792; average = 0·70787; Table 3) of the Ece and Faber travertines are in good agreement with the $^{87}Sr/^{86}Sr$ ratios reported by El Desouky *et al.* (2015) for the adjacent Çakmak quarry. These homogeneous $^{87}Sr/^{86}Sr$ values point to the involvement of one rather uniform fluid type for the Ballık area and suggest that Sr isotopes show no fractionation during dissolution of the substrate carbonates and reprecipitation as travertine. The Sr isotopic composition of the travertines thus reflects the signature of the dissolved parent carbonate sources (e.g. Minissale *et al.*, 2002). Based on a comparison between the Sr isotope ratio values of the travertines and the possible source rocks, El Desouky *et al.* (2015) suggested that the parent carbonate rock is probably the Triassic limestone of the Lycian Thrust Sheets.

The uppermost Oligocene to lower Miocene Acıdere carbonates and the upper Palaeocene to lower Eocene Dereköy carbonates (Sözbilir, 2005) have not been reported by El Desouky *et al.* (2015). Based on their limited geological and geographical distribution and slightly lower marine $^{87}Sr/^{86}Sr$ signatures (McArthur & Howarth, 2004), their influence is unlikely or very small.

The Sr isotope ratio data thus point to an important contribution of the carbonates of the Lycian Nappes in the supply of Ca^{2+} and HCO_3^- for subsequent travertine precipitation; they probably acted as the main subsurface water reservoir. The data also suggest that fluid–rock interaction with other rock units during fluid migration was minimal.

Stable carbon–oxygen isotopes

The Ece and Faber $\delta^{18}O$ values point to a meteoric origin of the fluids which could originate from surficial or shallow fluids, from a topographically driven deeper fluid or from diagenetic meteoric water. However, based on the Sr isotope ratio data, which point to a relatively deep origin, a purely surface meteoric water origin can be excluded. A scenario is envisaged in which infiltration of rain water occurs along the basin edges (mountains), and resurfaces along basin-bounding normal faults after having migrated through the reservoir (Fig. 20). Travertines could thus have precipitated from waters with a mixed topographically driven flow and surface origin or a relatively pure topographically driven flow origin with possible diagenetic overprinting.

Large-scale diagenetic alteration of the Ece and Faber travertines is limited. However, microscale evidence of recrystallization has been observed widely and could imply a resetting of the depositional stable isotopic signatures for the recrystallized fabrics. Recrystallization was interpreted as dominantly early diagenetic, related to the formation of acids as a consequence of organic decay (Chafetz & Folk, 1984) or the result of waters that partially percolated into pre-existing travertine deposits during on-going precipitation (Andrews & Brasier, 2005). For such conditions, $\delta^{18}O$ values and temperatures of the original and early diagenetic precipitating waters thus will have been practically the same, which is in agreement with the absence of variations in cathodoluminescence. Thus, it is suggested that the observed recrystallization had no major impact on the isotopic signatures. This suggestion is in line with the (limited) literature on possible diagenetic alteration of the stable isotopic signature in continental carbonates (e.g. Andrews & Brasier, 2005; Rainey & Jones, 2007).

Pentecost (2005) showed that $\delta^{18}O$ values of epigean meteogene (epigenic) and thermogene (endogenic) travertines generally plot in the same interval between $-3‰$ and $-10‰$ V-PDB. Based on the $\delta^{18}O$ results only, a purely topographically driven fluid flow versus a mixing origin with surface waters thus can neither be excluded, nor confirmed.

The $\delta^{13}C$ signature is the result of the relative contribution from the principal sources of dissolved CO_2 and HCO_3^- in the precipitating waters, but several processes can also have an impact on fractionation between the rocks and the fluids at stake. Panichi & Tongiorgi (1976) provided an empirical equation based on travertine analysis in Italy to recalculate the $\delta^{13}C$ of the CO_2 in the precipitating waters:

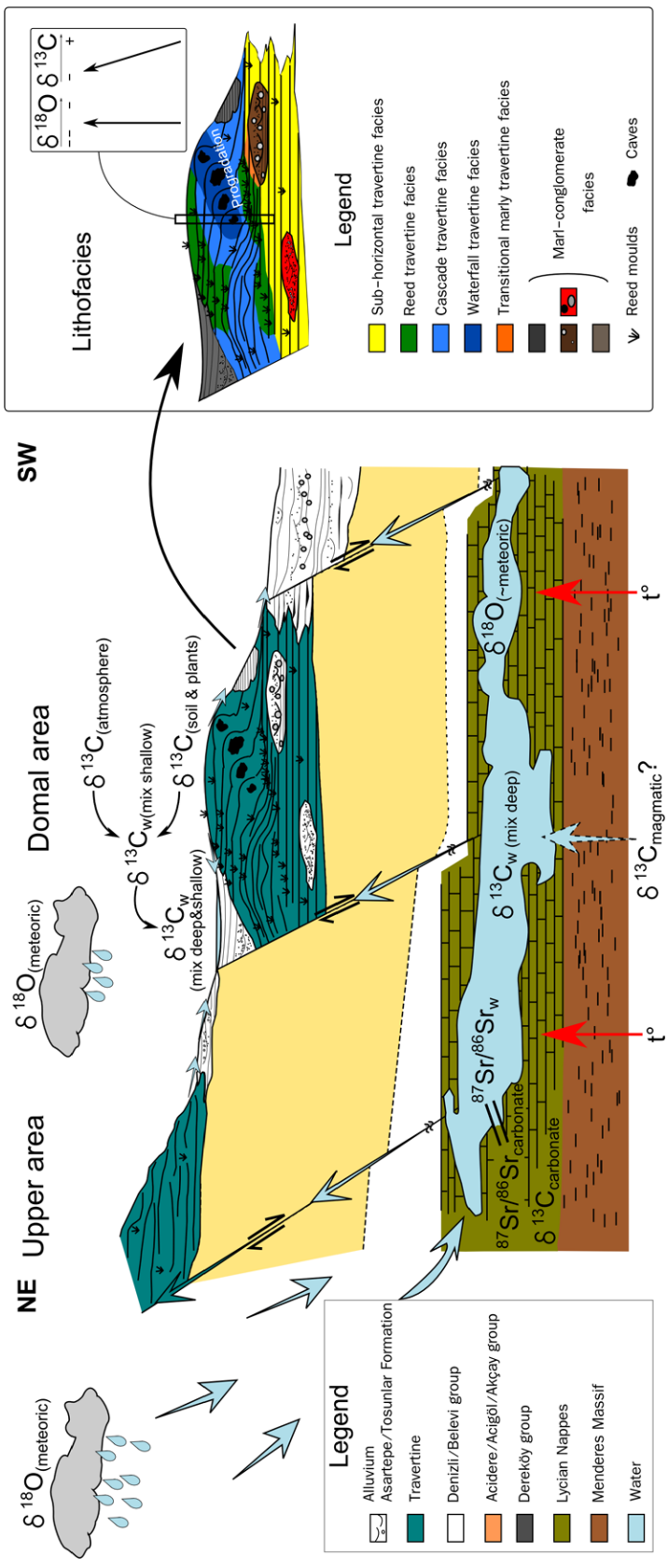

Fig. 20. Conceptual model combining sedimentology and geochemistry (not to scale). Infiltration of rain water occurs along the basin edges (mountains), and resurfaces along basin-bounding normal faults after having migrated through the reservoir. Travertines could thus have precipitated from waters with a mixed topographically driven flow and a surface origin or a relatively pure topographically driven flow origin with possible diagenetic overprinting. The travertine $\delta^{13}C$ and $\delta^{18}O$ signatures result from fractionation during precipitation from fluids with a mixed $\delta^{13}C$ and $\delta^{18}O$ composition. The $^{87}Sr/^{86}Sr$ ratio of the travertine will equal that of the precipitating fluids, and thus also that of the carbonate substrate rocks. Due to the long residence time of the fluids in the Lycian Nappes, their influence will dominate in the $^{87}Sr/^{86}Sr$ signatures. The meteoric signature of the waters is maintained both in shallow and deep waters.

$$\delta^{13}C_{CO_2} = 1{\cdot}2 \times \delta^{13}C_{trav} - 10{\cdot}5 \qquad (1)$$

Applying this equation to the Ece and Faber travertines results in $\delta^{13}C_{CO_2}$ values varying between −15·10‰ and −7·38‰, with a median value of −10·15‰. These results were compared to the signature of the possible sources (Fig. 21).

The $\delta^{13}C_{CO_2}$ probably reflects a complex mixture of different sources (Fig. 21) and should be combined with results from other techniques and literature for detailed interpretation. The results of the Sr isotope analysis indicate the Lycian Nappes as the main reservoir rocks with the estimated reservoir depth being *ca* 1000 m or less (Kele *et al.*, 2011). Based on Basel *et al.* (2010), the Lycian Nappes water reservoir temperature in the Denizli Basin would be up to 120°C. Estimated fractionation for 120°C, starting from $\delta^{13}C_{Bedrock}$ = +1·8‰ (Kele *et al.*, 2011), results in a $\delta^{13}C_{CO_2}$ of *ca* −1·2‰. Kele *et al.* (2011) concluded a thermometamorphic origin of the CO_2, which is in agreement with Özler (2000) and Şimşek *et al.* (2000). Güleç *et al.* (2002) reported that He isotopes for the Denizli area point to a contribution of magmatic CO_2. A mixing $\delta^{13}C$ signature of CO_2 from these different sources, even with possible atmospheric CO_2, will vary between +2‰ and −8‰, depending on their relative contribution. This is at least (and probably more than) 2·15‰ higher than the calculated value when using the formula of Panichi & Tongiorgi (1976).

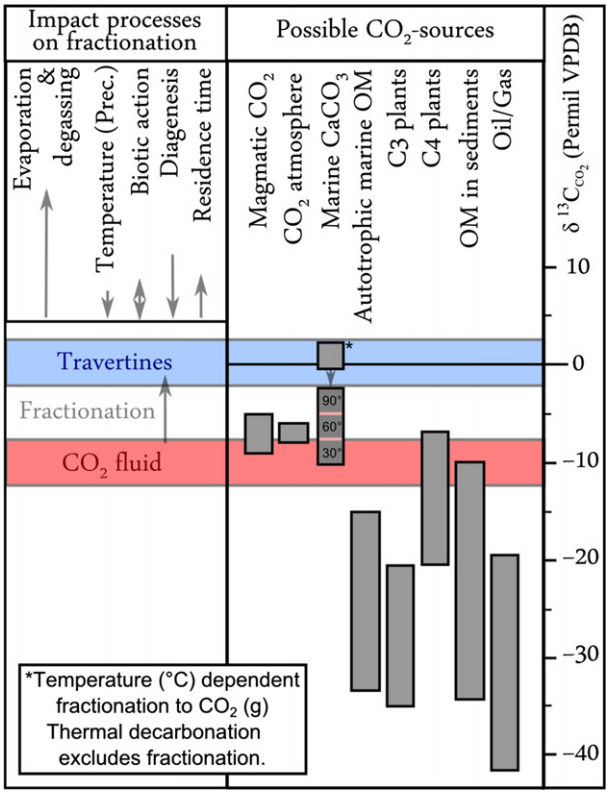

Fig. 21. Possible carbon dioxide sources and influencing processes on the $\delta^{13}C$ signatures of travertines (data from Deines *et al.*, 1974; Inoue & Sugimura, 1985; Andrews *et al.*, 1993, 1997; Rollinson, 1993; Sano & Marty, 1995; Rose & Davisson, 1996; Minissale *et al.*, 2002; Minissale, 2004; Sharp *et al.*, 2003; Leng & Marshall, 2004; Attanasio *et al.*, 2006; Uysal *et al.*, 2007; Hoefs, 2009; Jeandel *et al.*, 2010). Temperature dependent fractionation of marine carbonates based on Bottinga (1968) and Friedman & O'Neil (1977). Fractionation to travertine based on Panichi & Tongiorgi (1976). Arrows of impact processes are not to scale.

This difference could possibly be ascribed to properties and/or processes influencing fractionation (Fig. 21) such as precipitation temperature, diagenesis, biotic action, evaporation and degassing. The influence of the precipitation temperature on fractionation is small and the impact of diagenesis has already been ruled out. Biotic action could have played a role. The impact of microbial activity on the isotopic record is still subject to debate (e.g. Fouke *et al.*, 2000; Andrews & Riding, 2001; Fouke, 2001), but there is a consensus that the effect of degassing is more dominant in controlling the $\delta^{13}C$. When the precipitation environment is dominated by the presence of cyanobacteria or algae (for example, charophytes as identified by petrography; Fig. 4T), micro-environmental effects of photosynthesis should not be neglected (Andrews, 2006). The magnitude of microbial effects on the $\delta^{13}C$ signature could be up to 6‰ or 3‰ (Guo *et al.*, 1996; and Fouke *et al.*, 2000; respectively). Arp *et al.* (2010), however, also provide an example where the composition of the precipitates is not affected by photosynthesis-induced microgradrients. In-stream higher plant photosynthesis effects have been shown to be negligible (Usdowski *et al.*, 1979; Dandurand *et al.*, 1982; Spiro & Pentecost, 1991), except maybe in stagnant waters (Coletta *et al.*, 2001; Liu *et al.*, 2006). Despite the fact that the spring orifice of the Ece and Faber travertines is presently unknown, it is fair to assume that evaporation and degassing were the dominant processes that played a role after the waters surfaced. This implies that the general impact of these processes on the mixed $\delta^{13}C_{CO_2}$ would correspond to a positive trend (Fig. 21), clearly indicating that one or multiple CO_2 sources with light $\delta^{13}C$ values contributed to the

system. Organic matter or soil-related CO_2 seem the most plausible low $\delta^{13}C$ sources (Fig. 20). The vegetation in Turkey consists either of mixed C3/C4 plants or is dominated by C3 plants (Cerling & Quade, 1993), probably leading to strongly depleted $\delta^{13}C$ soils. Because these light carbons are most likely to be supplied by surface or shallow waters, the $\delta^{13}C$ signature of the travertines points to a mixing fluid origin.

While, based on the $\delta^{18}O$ signature only, no conclusions could be drawn on the possibility of mixing of deep topographically driven meteoric waters with surface meteoric waters, the $\delta^{13}C$ data are more straightforward. The $\delta^{13}C$ values support a contribution of both surface meteoric and deeply seated thermal CO_2. Thus there is a deeply derived significant water component involved in precipitation that allows these deposits to be considered as endogenic travertines (Crossey *et al.*, 2006). The reported data are in accordance with the micritic host rocks of the Çakmak quarry (El Desouky *et al.*, 2015) and the data for the most eastern part of the Ballık area provided by Özkul *et al.* (2013). This implies the same mixing palaeowaters and reservoir rocks for the whole Ballık area. A conceptual model is shown in Fig. 20.

The decreasing trend of the carbon isotope signature towards the top of the quarries, found in all lithostratigraphic sections (see Appendix S1), and thus occurring from the sub-horizontal, over the marl-conglomerate, cascade, waterfall and eventually to the reed facies, could reflect both an environmental variation as well as a temporal variation. The environmental variation suggests that the lithofacies and lithotypes are decisive for the stable isotopic signatures (cf. Kele *et al.*, 2008). Photosynthetic processes from higher plants in ponds and pools could explain the highest $\delta^{13}C$ values for the sub-horizontal facies, but then a similar shift would also be expected for the reed facies. Post-sedimentary soil formation processes for the reed facies could, however, have overprinted the plant isotopic effect.

Alternatively, the decreasing upward trend can be explained by the evolution in fluid composition with an increasing surface meteoric contribution with time. This would also be in agreement with the increasing plant mould abundance in the higher facies, compared to the sub-horizontal travertines.

A third possibility is the evolution from distal to more proximal deposits. Distal travertines precipitate from waters that are already significantly degassed, with preferential loss of light isotopes. The effect of degassing is known to be more pronounced for carbon than for oxygen. When the geochemical data are coupled with the sedimentary facies model (Fig. 20), this last possibility is appealing. The progradational nature of the system, with the progressive migration of the proximal deposits over the distal deposits, would explain the upwardly decreasing shift in $\delta^{13}C$ values.

Temperature calculations

For precipitation under isotopic equilibrium, the temperature of precipitation can be deduced based on the calcite–water $\delta^{18}O$ fractionation. However, isotopic equilibrium is rarely maintained under natural conditions during calcite precipitation in travertine settings (e.g. Fouke *et al.*, 2000; Coplen, 2007; Kele *et al.*, 2008, 2011; Özkul *et al.*, 2013, 2014). Although the exact position of the spring(s) of the Faber and Ece travertines is unknown and lies outside the quarries, both travertines can be interpreted as representing precipitation in a relatively distal position. Deviation from equilibrium precipitation is observed to be the highest at the spring vent, and to decrease with increasing distance from the spring orifice (Kele *et al.*, 2011). Precipitation temperatures of the Ece and Faber travertines will thus vary between the results obtained using the water–bicarbonate oxygen isotope fractionation equation of Halas & Wolacewicz (1982), and the results obtained for equilibrium by using the equation of Friedman & O'Neil (1977). Based on fluid inclusion and C–O isotopic analyses on cement samples from the Çakmak quarry, El Desouky *et al.* (2014) calculated the $\delta^{18}O_{water}$ to be $-5‰$ relative to the Vienna Standard Mean Ocean Water (V-SMOW) at Ballık. Accepting this value, the minimum temperature of the travertine precipitating fluid at Ece and Faber would have been somewhere between 18°C and 26·5°C, whereas the maximum temperature plots between 36°C and 46°C. The mean isotopic signature results in a temperature between 26°C and 35°C. These results are consistent with the temperature range of 23 to 39°C that was calculated by Özkul *et al.* (2013).

CONCLUSIONS

A detailed sedimentological, diagenetic and geochemical investigation of the Ece and Faber travertines was executed. Based on detailed line

drawings, the constructed depositional three-dimensional model provides a unique insight into the internal sedimentological Ballık travertine dome architecture. The general progradation of the system is apparent as sigmoidal clinoforms with downlap terminations. Four main travertine lithofacies and 15 main lithotypes were described. Peloidal, phyto and dendritic lithotypes dominate the Ece and Faber travertines. Based on petrographic and environmental scanning electron microscope (E-SEM) observations and comparison with literature, microbial communities in the form of mats or biofilms probably acted as nucleation mediators before physico-chemical precipitation took over. The environment of travertine precipitation evolved from a dominantly sub-aqueous to a dominantly sub-aerial environment, as represented by the sub-horizontal and biostromal reed travertine facies and the cascade, waterfall and biohermal reed travertine facies, respectively. The boundary between these two systems is indicated by the incursion of the marl-conglomerate facies, which reflects a lacustrine system, temporarily interrupted and cut by rivers. Without further information on the location of the vent and the age of travertine deposition, no conclusions can be drawn in favour of an intrinsic or extrinsic cause for this incursion. Riverine and palustrine–lacustrine siliciclastics form the lateral and covering facies of the travertine dome.

Large-scale diagenetic alteration of the Ece and Faber travertines was limited, as inferred from the lack of extensive macroscopic cementation or dissolution. Petrographically observed recrystallization was mainly syn-depositional to early diagenetic, not resulting in significant changes for the original stable isotopic signature. Strontium and stable oxygen–carbon isotope signatures of the travertines point to a mixing mechanism of palaeofluids with deeply originated heavy carbon CO_2 and lighter carbon CO_2 of a shallow origin. The relative contribution of the stable carbon isotopes seems to be environmentally controlled. The Triassic Lycian Nappes acted as the main parent carbonate rock. The Ece and Faber travertines can thus be considered as endogenic travertines, in which regardless of the water temperature, a deeply derived significant water component is involved in precipitation (Crossey *et al.*, 2006).

The unique reconstruction of the Ballık travertine dome can potentially serve as an analogue for sub-surface, offshore travertine geobodies, like for example the domal carbonate build-ups in the Pre-Salt of the Atlantic. In combination with petrophysical and acoustic data (Soete *et al.*, 2015), the here presented lithofacies geobody model can form the basis for future reservoir analogue and acoustic modelling.

ACKNOWLEDGEMENTS

Thanks go to M. Joachimski and colleagues of the Friedrich-Alexander-Universität (Erlangen-Nürnberg, Germany) for performing the oxygen-carbon stable isotope measurements and to R. De Vos from the Department of Metallurgy and Materials Engineering of the KU Leuven (Belgium) for E-SEM images. K. Latruwe is thanked for help with the ICP-QMS and MC-ICP-MS instruments. H. Nijs is acknowledged for the preparation of thin-sections and A. Foubert for help during fieldwork. We are grateful to TOTAL, ENI E&P and PETROBRAS for funding this project. The suggestions of Associate Editor J. Reijmer and reviewers A. Brasier and G. Della Porta were strongly appreciated and helped to improve the manuscript.

REFERENCES

Alçiçek, H., **Varol, B.** and **Özkul, M.** (2007) Sedimentary facies, depositional environments and palaeogeographic evolution of the Neogene Denizli Basin, SW Anatolia, Turkey. *Sed. Geol.*, **202**, 596–637.

Amieux, P., **Bernier, P.**, **Dalongeville, R.** and **Medwecki, V.** (1989) Cathodoluminescence of carbonate-cemented Holocene beachrock from Togo coastline (West Africa): an approach to early diagenesis. *Sed. Geol.*, **65**, 261–272.

Andrews, J.E. (2006) Palaeoclimatic records from stable isotopes in riverine tufas: synthesis and review. *Earth Sci. Rev.*, **75**, 85–104.

Andrews, J.E. and **Brasier, A.T.** (2005) Seasonal records of climatic change in annually laminated tufas: short review and future prospects. *J. Quat. Sci.*, **20**, 411–421.

Andrews, J.E. and **Riding, R.** (2001) Depositional facies and aqueous-solid geochemistry of travertine-depositing hot springs (Angel Terrace, Mammoth Hot Springs, Yellowstone National Park, U.S.A.) – Discussion. *J. Sediment. Res.*, **71**, 496–497.

Andrews, J.E., **Riding, R.** and **Dennis, P.F.** (1993) Stable isotopic compositions of recent freshwater cyanobacterial carbonates from the British Isles: local and regional environmental controls. *Sedimentology*, **40**, 303–314.

Andrews, J.E., **Riding, R.** and **Dennis, P.F.** (1997) The stable isotope record of environmental and climatic signals in modern terrestrial microbial carbonates from Europe. *Palaeogeogr. Palaeoclimatol. Palaeoecol.*, **129**, 171–189.

Arp, G., **Bissett, A.**, **Brinkmann, N.**, **Cousin, S.**, **De Beer, D.**, **Friedl, T.**, **Mohr, K.I.**, **Neu, T.R.**, **Reimer, A.**, **Shiraishi, F.**, **Stackebrandt, E.** and **Zippel, B.** (2010) Tufa-forming

biofilms of German karstwater streams: microorganisms, exopolymers, hydrochemistry and calcification. In: *Tufas and Speleothems: Unravelling the Microbial and Physical Controls* (Eds H.M. Pedley and M. Rogerson), *Geol. Soc. London. Spec. Publ.*, **336**, 93–118.

Attanasio, D., **Brilli, M.** and **Ogle, N.** (2006) *The Isotopic Signature of Classical Marble*. L'Erma di Bretschneider, Rome, 297 pp.

Barilaro, F., **Della Porta, G.** and **Cappezuoli, E.** (2012) Depositional geometry and fabric types of hydrothermal travertine deposits (Albegna Valley, Tuscany, Italy). *Rend. Soc. Geol. Ital.*, **21**, 1024–1025.

Basel, E.D.K., **Serpen, U.** and **Satman, A.** (2010) Turkey's geothermal energy potential: updated results. *Proceedings, Thirty-Fifth Workshop on Geothermal Reservoir Engineering*, Stanford University, Stanford, California, February 1-3, 2010.

Bottinga, Y. (1968) Calculation of fractionation factors for carbon and oxygen in the system calcite–carbon dioxide–water. *J. Phys. Chem.*, **72**, 800–808.

Bozkurt, E. (2001) Neotectonics of Turkey — a synthesis. *Geodin. Acta*, **14**, 3–30.

Brasier, A.T. (2011) Searching for travertines, calcretes and speleothems in deep time: processes, appearances, predictions and the impact on plants. *Earth Sci. Rev.*, **104**, 213–239.

Brasier, A.T., **Andrews, J.E.** and **Kendall, A.C.** (2011) Diagenesis or dire genesis? The origin of columnar spar in tufa stromatolites of Central Greece and the role of chironomid larvae *Sedimentology*, **58**, 1283–1302.

Buckley, J.P., **Elders, C.** and **Mann, J.** (2013) Carbonate Buildups in the Santos Basin, Offshore Brazil. Programme and abstract volume: microbial carbonates in space and time: implications for global exploration and production. *Geol. Soc.*, 37–38. 19–20 June, 2013.

Capezzuoli, E., **Gandin, A.** and **Pedley, M.** (2014) Decoding tufa and travertine (fresh water carbonates) in the sedimentary record: the state of the art. *Sedimentology*, **61**, 1–21.

Casanova, J., **Bodénan, F.**, **Négrel, P.** and **Azaroual, M.** (1999) Microbial control on the precipitation of modern ferrihydrite and carbonate deposits from the Cézallier hydrothermal springs (Massif Central, France). *Sed. Geol.*, **126**, 125–145.

Cerling, T.E. and **Quade, J.** (1993) Stable carbon and oxygen isotopes in soil carbonates. In: *Climate Change in Continental Isotopic Records* (Eds P.K. Swart, K.C. Lohmann, J. McKenzie and S. Savin), pp. 1–36. Geophysical Monograph 78, American Geophysical Union, Washington, DC.

Chafetz, H.S. (2013) Porosity in bacterially induced carbonates: focus on micropores. *AAPG Bull.*, **97**, 2103–2111.

Chafetz, H.S. and **Folk, R.L.** (1984) Travertines: depositional morphology and the bacterially-constructed constituents. *J. Sed. Petrol.*, **54**, 289–316.

Chafetz, H.S. and **Guidry, S.A.** (1999) Bacterial shrubs, crystal shrubs, and ray-crystal crusts: bacterially induced vs. abiotic mineral precipitation. *Sed. Geol.*, **126**, 57–74.

Chafetz, H.S., **Srdoc, D.** and **Horvatincic, N.** (1994) Early diagenesis of Plitvice lakes waterfall and barrier travertine deposits. *Géog. Phys. Quatern.*, **48**, 247–255.

Cobanoğlu, I. and **Çelik, S.B.** (2012) Determination of strength parameters and quality assessment of Denizli travertines (SW Turkey). *Eng. Geol.*, **129–130**, 38–47.

Coletta, P., **Pentecost, A.** and **Spiro, B.** (2001) Stable isotopes in charophyte incrustations: relationships with climate and water chemistry. *Palaeogeogr. Palaeoclimatol. Palaeoecol.*, **173**, 9–19.

Collins, A.S. and **Robertson, A.H.F.** (1997) Lycian melange, southwestern Turkey: an emplaced Late Cretaceous accretionary complex. *Geology*, **25**, 255–258.

Collins, A.S. and **Robertson, A.H.F.** (1998) Processes of Late Cretaceous to Late Miocene episodic thrust sheet translation in the Lycian Taurides, SW Turkey. *J. Geol. Soc. London*, **155**, 759–772.

Coplen, T.B. (2007) Calibration of the calcite-water oxygen-isotope geothermometer at Devils Hole, Nevada, a natural laboratory. *Geochim. Cosmoschim. Acta*, **71**, 3948–3957.

Crossey, L.J., **Fischer, T.P.**, **Patchett, J.P.**, **Karlstrom, K.E.**, **Hilton, D.R.**, **Newell, D.L.**, **Huntoon, P.**, **Reynolds, A.C.** and **de Leeuw, G.A.M.** (2006) Dissected hydrologic system at the Grand Canyon: interaction between deeply derived fluids and plateau aquifer waters in modern springs and travertine. *Geology*, **34**, 25–28.

Dandurand, J.L., **Gout, R.**, **Hoefs, J.**, **Menschel, G.**, **Schott, J.** and **Usdowski, E.** (1982) Kinetically controlled variations of major components and carbon and oxygen isotopes in a calcite-depositing spring. *Chem. Geol.*, **36**, 299–315.

De Filippis, L., **Faccenna, C.**, **Billi, A.**, **Anzalone, E.**, **Brilli, M.**, **Özkul, M.**, **Soligo, M.**, **Tuccimei, P.** and **Villa, I.M.** (2012) Growth of fissure ridge travertines from geothermal springs of Denizli Basin, western Turkey. *Geol. Soc. Am. Bull.*, **124**, 1629–1645.

De Fillippis, L., **Facenna, C.**, **Billi, A.**, **Anzalone, E.**, **Brilli, M.**, **Soligo, M.** and **Tuccimei, P.** (2013) Plateau versus fissure ridge travertine from Quaternary geothermal springs of Italy and Turkey: interactions and feedbacks between fluid discharge, palaeoclimate, and tectonics. *Earth Sci. Rev.*, **123**, 35–52.

De Muynck, D., **Huelga-Suarez, G.**, **Van Heghe, L.**, **Degryse, P.** and **Vanhaecke, F.** (2009) Systematic evaluation of a strontium-specific extraction chromatographic resin for obtaining a purified Sr fraction with quantitative recovery from complex and Ca-rich matrices. *J. Anal. At. Spectrom.*, **24**, 1498–1510.

Défarge, C., **Trichet, J.**, **Jaunet, A.M.**, **Rober, M.**, **Tribble, J.** and **Sansone, F.J.** (1996) Texture of microbial sediments revealed by cryo-scanning electron microscopy. *J. Sediment. Res.*, **66**, 935–947.

Deines, P., **Langmuir, D.** and **Harmon, R.S.** (1974) Stable carbon isotope ratios and the existence of a gas phase in the evolution of carbonate groundwaters. *Geochim. Cosmochim. Acta*, **38**, 1147–1164.

Dupraz, C., **Visscher, P.T.**, **Baumgartner, L.K.** and **Reid, R.P.** (2004) Microbe–mineral interactions: early carbonate precipitation in a hypersaline lake (Eleuthera Island, Bahamas). *Sedimentology*, **51**, 745–765.

El Desouky, H., **Soete, J.**, **Claes, H.**, **Özkul, M.**, **Vanhaecke, F.** and **Swennen, R.** (2015) Novel applications of fluid inclusions and isotope geochemistry in unravelling the genesis of fossil travertine systems. *Sedimentology*, **62**, 27–56.

Engin, B. and **Güven, O.** (1997) Thermoluminescence Dating of Denizli Travertines from the Southwestern Part of Turkey. *Appl. Radiat. Isot.*, **48**, 1257–1264.

Erten, H., **Sen, S.** and **Özkul, M.** (2005) Pleistocene mammals from travertine deposits of the Denizli Basin (SW Turkey). *Ann. Paleontol.*, **91**, 267–278.

Folk, R.L. and **Chafetz, H.S.** (1983) Pisoliths (pisoids) in Quaternary travertines of Tivoli, Italy. In: *Coated Grains* (Ed. T.M. Peyt), pp. 474–487. Springer-Verlag, Berlin Heidelberg.

Folk, R.L., **Chafetz, H.S.** and **Tiezzi, P.A.** (1985) Bizarre forms of depositional and diagenetic calcite in hot spring travertines, central Italy. In: *Carbonate Cements* (Ed. N. Scheidemann and P. Harris), *Spec. Publ. Soc. Econ. Paleont. Miner.*, **36**, 349–369.

Ford, T.D. and **Pedley, H.M.** (1996) A review of tufa and travertine deposits of the world. *Earth Sci. Rev.*, **41**, 117–175.

Fouke, B.W. (2001) Depositional facies and aqueous-solid geochemistry of travertine-depositing hot springs (Angel Terrace, Mammoth Hot Springs, Yellowstone National Park, U.S.A.) – Reply. *J. Sediment. Res.*, **71**, 497–500.

Fouke, B.W. (2011) Hot-spring Geobiology: abiotic and biotic influence on travertine formation at Mammoth Hot Springs, Yellowstone National Park, USA. *Sedimentology*, **58**, 170–219.

Fouke, B.W., **Farmer, J.D.**, **Des Marais, D.D.**, **Pratt, L.**, **Sturchio, N.C.**, **Burns, P.C.** and **Discipulo, M.K.** (2000) Depositional facies and aqueous-solid geochemistry of travertine-depositing hot springs (Angel Terrace, Mammoth Hot Springs, Yellowstone National Park, U.S.A.). *J. Sediment. Res.*, **70**, 565–585.

Friedman, I. and **O'Neil, J.R.** (1977) Chapter KK. Compilation of stable isotope fractionation factors of geochemical interest. In: *Data of Geochemistry* (Ed. M. Fleischer), 6th edn, *Geol. Surv. Prof. Pap. 440*, KK1–KK12.

Glime, J.M. and **Vitt, D.H.** (1984) Physiological adaption of aquatic Musci. *Lindbergia*, **10**, 41–52.

Golubic, S. (1969) Cyclic and noncyclic mechanisms in the formation of travertine. *Verh. Int. Ver. Limnol.*, **17**, 956–961.

Golubic, S., **Violante, C.**, **Plenkovic-Moraj, A.** and **Grgasovic, T.** (2008) Travertines and calcareous tufa deposits: an insight into diagenesis. *Geol. Croatia*, **61**, 363–378.

Güleç, N., **Hilton, D.R.** and **Mutlu, H.** (2002) Helium isotope variations in Türkey: relationship to tectonics, volcanism and recent seismic activities. *Chem. Geol.*, **187**, 129–142.

Gündoğan, İ., **Helvaci, C.** and **Sözbilir, H.** (2008) Gypsiferous carbonates at Honaz Dağı (Denizli): first documentation of Triassic gypsum in western Turkey and its tectonic significance. *J. Asian Earth Sci.*, **32**, 49–65.

Guo, L. and **Riding, R.** (1992) Aragonite laminae in hot water travertine crusts, Rapolane Terme, Italy. *Sedimentology*, **39**, 1067–1079.

Guo, L. and **Riding, R.** (1994) Origin and diagenesis of Quaternary travertine shrub fabrics, Rapolano Terme, central Italy. *Sedimentology*, **41**, 499–520.

Guo, L. and **Riding, R.** (1998) Hot-spring travertine facies and sequences, Late Pleistocene, Rapolano Terme, Italy. *Sedimentology*, **45**, 163–180.

Guo, L., **Andrews, J.**, **Riding, R.**, **Dennis, P.** and **Dresser, Q.** (1996) Possible microbial effects on stable carbon isotopes in hot-spring travertines. *J. Sediment. Res.*, **66**, 468–473.

Gürbüz, A., **Boyraz, S.** and **Ismael, M.T.** (2012) Plio-Quaternary development of the Baklan-Dinar graben: implications for cross-graben formation in SW Turkey. *Int. Geol. Rev.*, **54**, 33–50.

Halas, S. and **Wolacewicz, W.** (1982) The experimental study of oxygen isotope exchange reaction between dissolved bicarbonate and water. *J. Chem. Phys.*, **76**, 5470–5472.

Hancock, P.L., **Chalmers, M.L.**, **Altunel, E.**, **Cakir, Z.** and **Becher-Hancock, A.** (2000) Creation and destruction of travertine monumental stone by earthquake faulting at Hierapolis, Turkey. *Geol. Soc. London. Spec. Publ.*, **171**, 1–14.

van Hinsbergen, D.J.J., **Kaymakci, N.**, **Spakman, W.** and **Torsvik, T.H.** (2010) Reconciling the geological history of western Turkey with plate circuits and mantle tomography. *Earth Planet. Sci. Lett.*, **297**, 674–686.

Hoefs, J. (2009) *Stable Isotope Geochemistry*. Springer-Verlag, Berlin, 285 pp.

Inoue, H. and **Sugimura, Y.** (1985) Carbon isotopic fractionation during the CO_2 exchange process between air and sea water under equilibrium and kinetic conditions. *Geochim. Cosmochim. Acta*, **49**, 2453–2460.

Janssen, A. (2000) Petrography and geochemistry of active and fossil tufa deposits from Belgium. Thesis presented in pursuit of the degree of Doctor in Sciences, Department Geography-Geology, Faculty of Sciences, Katholieke Universiteit Leuven, 1999-2000.

Janssen, A., **Swennen, R.**, **Podoor, N.** and **Keppens, E.** (1999) Biological and diagenetic influence in recent and fossil tufa from Belgium. *Sed. Geol.*, **126**, 74–95.

Jeandel, E., **Battani, A.** and **Sarda, P.** (2010) Lessons from natural and industrial analogues for storage of carbon dioxide. *Int. J. Greenhouse Gas Control*, **4**, 890–909.

Jones, B. and **Kahle, C.F.** (1986) Dendritic calcite crystals formed by calcification of algal filaments in a vadose environment. *J. Sed. Petrol.*, **56**, 217–227.

Jones, B., **Renaut, R.W.** and **Rosen, M.R.** (2000) Trigonal dendritic calcite crystals forming from hot spring waters at waikite, North Island, New Zealand. *J. Sediment. Res.*, **70**, 586–603.

Kallis, P., **Bleich, K.E.** and **Stahr, K.** (2000) Micromorphological and geochemical characterization of Tertiary 'freshwater carbonates' locally preserved north of the edge of the Miocene Molasse Basin (SW Germany). *Catena*, **41**, 19–42.

Kappelman, J., **Alçiçek, M.C.**, **Kazancı, N.**, **Schultz, M.**, **Özkul, M.** and **Şevket, Ş.** (2008) Brief communication: first Homo erectus from Turkey and implications for migrations into temperate Eurasia. *Am. J. Phys. Anthropol.*, **135**, 110–116.

Kaypak, B. and **Gökkaya, G.** (2012) 3-D imaging of the upper crust beneath the Denizli geothermal region by local earthquake tomography, western Turkey. *J. Volcanol. Geoth. Res.*, **211–212**, 47–60.

Kele, S., **Demény, A.**, **Siklósy, Z.**, **Németh, T.**, **Tóth, M.** and **Kovács, M.B.** (2008) Chemical and stable isotope composition of recent hot-water travertines and associated thermal waters, from Egerszalók, Hungary: depositional facies and non-equilibrium fractionation. *Sed. Geol.*, **211**, 53–72.

Kele, S., **Özkul, M.**, **Fórizs, I.**, **Gökgöz, A.**, **Baykara, M.O.**, **Alçiçek, M.C.** and **Németh, T.** (2011) Stable isotope geochemical and facies study of Pamukkale travertines: new evidences of low temperature non-equilibrium calcite-water fractionation. *Sed. Geol.*, **238**, 191–212.

Khatib, S., **Rochette, P.**, **Alçiçek, M.C.**, **Lebatard, A.E.**, **Demory, F.** and **Saos, T.** (2014) Etudes stratigraphique, sédimentologique et paléomagnétique des travertins de Kocabaş, Bassin de Denizli, Anatolie, Turquie, contenant des restes fossiles quaternaires. *L'anthropologie*, **118**, 16–33.

Konak, N. and **Senel, M.** (2002) *Geological Map of Turkey, Denizli Sheet 1:500 000*. Maden Tetkik ve Arama Genel Müdürlügü, Ankara.

Lebatard, A.E., **Alçiçek, M.C.**, **Rochette, P.**, **Khatib, S.**, **Vialet, A.**, **Boulbes, N.**, **Bourlès, D.L.**, **Demory, F.**, **Guipert, G.**, **Mayda, S.**, **Titov, V.V.**, **Vidal, L.** and **de Lumley, H.** (2014) Dating the Homo erectus bearing travertine from Kocabaş (Denizli, Turkey) at at least 1.1 Ma. *Earth Planet. Sci. Lett.*, **390**, 8–18.

Leng, M.J. and **Marshall, J.D.** (2004) Paleoclimate interpretation of stable isotope data from lake sediment archives. *Quatern. Sci. Rev.*, **23**, 811–831.

Liu, Z., **Li, Q.**, **Sun, H.**, **Liao, C.**, **Li, H.**, **Wang, J.** and **Wu, K.** (2006) Diurnal variations of hydrochemistry in a travertine-depositing stream at Baishuitai, Yunnan, SW China. *Aquat. Geochem.*, **12**, 103–121.

Love, K.M. and **Chafetz, H.S.** (1988) Diagenesis of laminated travertine crusts, Arbuckle Mountains, Oklahoma. *J. Sediment. Petrol.*, **58**, 441–445.

Machel, H. (2000) Application of cathodoluminescence to carbonate diagenesis. In: *Cathodoluminescence in Geosciences* (Eds M. Pagel, V. Barbin, P. Blanc and D. Ohnenstetter), pp. 271–301. Springer-Verlag, Berlin Heidelberg.

Machel, H.G., **Mason, R.A.**, **Mariano, A.N.** and **Mucci, A.** (1991) Causes and emission of luminescence in calcite and dolomite. In: *Luminescence Microscopy and Spectroscopy – Qualitative and quantitative applications* (Eds C.E. Barker and O.C. Kopp), pp. 9–25, *SEPM* Short Course, **25**, 9–25.

Mallick, R. and **Frank, N.** (2002) A new technique for precise uranium-series dating of travertine micro-samples. *Geochim. Cosmochem. Acta*, **66**, 4261–4272.

McArthur, J.M. and **Howarth, R.J.** (2004) Sr-isotope stratigraphy: the Phanerozoic $^{87}Sr/^{86}Sr$-curve and explanatory notes. In: *A Geological Timescale* (Eds F. Gradstein, J. G. Ogg and A.G. Smith), pp. 96–105. Cambridge University press, Mouscron.

Minissale, A. (2004) Origin, transport and discharge of CO_2 in central Italy. *Earth-Sci. Rev.*, **66**, 89–141.

Minissale, A., **Kerrick, D.M.**, **Magro, G.**, **Murrell, M.T.**, **Paladini, M.**, **Rihs, S.**, **Sturchio, N.C.**, **Tassi, F.** and **Vaselli, O.** (2002) Geochemistry of Quaternary travertines in the region north of Rome (Italy): structural, hydrologic and paleoclimatologic implications. *Earth Planet. Sci. Lett.*, **203**, 709–728.

Özkul, M., **Varol, B.** and **Alçiçek, M.C.** (2002) Depositional environments and petrography of Denizli travertines. *Bull. Mineral Res. Explor.*, **125**, 13–29.

Özkul, M., **Engin, B.**, **Alçiçek, M.C.**, **Koralay, T.** and **Demirtas, H.** (2004) Thermoluminescence dating of Quaternary hot spring travertines and some implications on graben evolution, Denizli, Western Turkey. 32nd International Geological Congress, August 20–28, Florence, Italy, p. 1474.

Özkul, M., **Gökgöz, A.** and **Horvatincic, N.** (2010) Depositional properties and geochemistry of Holocene perched springline tufa deposits and associated spring waters: a case study from the Denizli province, Western Turkey. In: *Tufas and Speleothems: Unravelling the Microbial and Physical Controls* (Eds H.M. Pedley and M. Rogerson), pp. 245–262. *Geol. Soc. London*, **336**, 245–262.

Özkul, M., **Kele, S.**, **Gökgöz, A.**, **Shen, C.C.**, **Jones, B.**, **Baykara, M.O.**, **Fórizs, I.**, **Németh, T.**, **Chang, Y.-W.** and **Alçiçek, M.C.** (2013) Comparison of the Quaternary travertine sites in the Denizli Extensional Basin based on their depositional and geochemical data. *Sed. Geol.*, **294**, 179–204.

Özkul, M., **Gökgöz, A.**, **Kele, S.**, **Baykara, M.O.**, **Shen, C.-C.**, **Chang, Y.-W.**, **Kaya, A.**, **Hançer, M.**, **Aratman, C.**, **Akın, T.** and **Örü, Z.** (2014) Sedimentological and geochemical characteristics of a fluvial travertine: a case from the eastern Mediterranean region. *Sedimentology*, **61**, 291–318.

Özler, H.M. (2000) Hydrogeology and geochemistry in the Curuksu (Denizli) hydrothermal field, western Turkey. *Environ. Geol.*, **39**, 1169–1180.

Panichi, C. and **Tongiorgi, E.** (1976) Carbon isotopic composition of CO_2 from springs, fumaroles, mofettes and travertines of central and southern Italy: a preliminary prospection method of geothermal areas. *Proceedings of the 2nd U.N. Symposium on the Development and Use of Geothermal Energy*, San Francisco, 20–29 May 1975, 815–825

Pedley, H.M. (1990) Classification and environmental models of cool freshwater tufas. *Sed. Geol.*, **68**, 143–154.

Pedley, H.M. and **Rogerson, M.** (2010) Tufas and speleothems: unravelling the microbial and physical controls. *Geol. Soc. London. Spec. Publ.*, **336**, 362.

Pedley, H.M., **Ordonez, S.**, **Gonzales-Martin, J.A.** and **Garcia Del Cura, M.A.** (2003) Sedimentology of Quaternary perched springline and paludal tufas: criteria for recognition, with examples from Guadalajara Province, Spain. *Sedimentology*, **50**, 23–44.

Pentecost, A. (2005) *Travertine*. Springer-Verlag, Berlin Heidelberg. 445 pp.

Rainey, D.K. and **Jones, B.** (2007) Rapid cold water formation and recrystallization of relict bryophyte tufa at the Fall Creek cold springs, Alberta, Canada. *Can. J. Earth Sci.*, **44**, 889–909.

Richter, D.K. and **Zinkernagel, U.** (1981) Zur Anwendung der Kathodolumineszenz in der Karbonatpetrographie. *Geol. Rundsch.*, **70**, 1276–1302.

Riding, R. (1991) Classification of microbial carbonates. In: *Calcareous Algae and Stromatolites* (Ed. R. Riding), pp. 21–51. Springer-Verlag, Berlin.

Riding, R. (2000) Microbial carbonates: the geological record of calcified bacterial-algal mats and biofilms. *Sedimentology*, **47**(Suppl. 1), 179–214.

Rogerson, M., **Pedley, H.M.**, **Wadhawan, J.D.** and **Middleton, R.** (2008) New insights into biological influence on the geochemistry of freshwater carbonate deposits. *Geochim. Cosmochim. Acta*, **72**, 4976–4987.

Rollinson, H.R. (1993) *Using Geochemical Data: Evaluation, Presentation, Interpretation*, Longman Geochemistry Series. Longman Group UK Limited, Pearson Education Limited, Oxfordshire, UK.

Rose, T.P. and **Davisson, M.L.** (1996) Radiocarbon in hydrologic systems containing dissolved magmatic carbon dioxide. *Science*, **273**, 1367–1370.

Sano, Y. and **Marty, B.** (1995) Origin of carbon in fumarolic gas from island arcs. *Chem. Geol.*, **119**, 265–274.

Sant'Anna, L.G., **Riccomini, C.**, **Rodrigues-Francisco, B.H.**, **Sial, A.N.**, **Carvalho, M.D.** and **Moura, C.A.V.** (2004) The Paleocene travertine system of the Itaboraí basin, Southeastern Brazil. *J. S. Am. Earth Sci.*, **18**, 11–25.

Selley, R.C. (1985) *Sedimentary environments and facies in Ancient Sedimentary Environments*, 3rd edn. Cornell University Press, Ithaca, NY, 317 pp.

Sharp, Z.D., **Papike, J.J.** and **Durakiewicz, T.** (2003) The effect of thermal decarbonation on stable isotope compositions of carbonates. *Am. Mineral.*, **88**, 87–92.

Sharp, I., **Verwer, K.**, **Ferreira, H.**, **Lapponi, F.**, **Snidero, M.**, **Machado, V.**, **Holtar, E.**, **Swart, R.**, **Marsh, J.**, **Gindre, L.**, **Puigdefabregas, C.** and **Fejerskov, M.** (2013) Pre- and Post-Salt Non-Marine Carbonates of the Namibe Basin, Angola. Programme and abstract volume: microbial carbonates in space and time: implications for global exploration and production.*Geol. Soc.*, **52**, 19–20 June, 2013.

Sierralta, M., **Kele, S.**, **Melcher, F.**, **Hambach, U.**, **Reinders, J.**, **van Gelderen, R.** and **Frechen, M.** (2010) Uranium-series dating of travertine from Süttő: implications for reconstruction of environmental change in Hungary. *Quatern. Int.*, **222**, 178–193.

Şimşek, S., **Guè Nay, G.**, **Elhatip, H.** and **Ekmekçi, M.** (2000) Environmental protection of geothermal waters and travertines at Pamukkale, Turkey. *Geothermics*, **29**, 557–572.

Şimşek, Ş., **Yildirim, N.** and **Gülgör, A.** (2005) Developmental and environmental effects of the Kizildere geothermal power project, Turkey. *Geothermics*, **34**, 234–251.

Soete, J., **Kleipool, L.M.**, **Claes, H.**, **Claes, S.**, **Hamaekers, H.**, **Özkul, M.**, **Foubert, A.**, **Reijmer, J.J.G.** and **Swennen, R.** (2015) Acoustic properties in travertines and their relation to porosity and pore types. *Mar. Pet. Geol.*, **59**, 320–335.

Sözbilir, H. (2002) Revised stratigraphy and facies analysis of Palaeocene-Eocene supra–allochthonous sediments (Denizli, SW-Turkey) and their tectonic significance. *Turk. J. Earth Sci.*, **11**, 87–112.

Sözbilir, H. (2005) Oligo-Miocene extension in the Lycian orogen: evidence from the Lycian molasse basin, SW Turkey. *Geodin. Acta*, **18**, 255–282.

Spiro, B. and **Pentecost, A.** (1991) One day in the life of a stream – a diurnal inorganic carbon mass balance for a travertine-depositing stream (Waterfall beck, Yorkshire). *Geomicrobiol J.*, **9**, 1–11.

Terra, G.J.S., **Spadini, A.R.**, **França, A.B.**, **Sombra, C.L.**, **Zambonato, E.E.**, **Juschaks, L.C.d.S.**, **Arienti, L.M.**, **Erthal, M.M.**, **Blauth, M.**, **Franco, P.P.**, **Matsuda, N.S.**, **da Silva, N.G.C.**, **Junior, P.A.M.**, **D'Avila, R.S.F.**, **deSouza, R.S.**, **Tonietto, S.N.**, **dos Anjos, S.M.C.**, **Campinho, V.S.** and **Winter, W.R.** (2010) Classificação de rochas carbonáticas aplicacável às bacias sedimentares brasileiras. Carbonate rock classification applied to brazilian sedimentary basins. *B. Geoci. Petrobras, Rio de Janeiro*, **18**, 9–29.

Thirlwall, M.F. (1991) Long-term reproducibility of multicollector Sr and Nd isotope ratio analysis. *Chem. Geol.*, **94**, 85–104.

Turner, E.C. and **Jones, B.** (2005) Microscopic calcite dendrites in cold-water tufa: implications for nucleation of micrite and cement. *Sedimentology*, **52**, 1043–1066.

Usdowski, E., **Hoefs, J.** and **Menschel, G.** (1979) Relationship between 13C and 18O fractionation and changes in major element composition in a recent calcite-depositing spring – a model of chemical variations with inorganic CaCO3 precipitation. *Earth Sci Planet. Lett.*, **42**, 267–276.

Uysal, T., **Feng, Y.**, **Zhao, J.**, **Altunel, E.**, **Weatherley, D.**, **Karabacak, V.**, **Cengiz, O.**, **Golding, S.D.**, **Lawrence, M.G.** and **Collerson, K.D.** (2007) U-series dating and geochemical tracing of late Quaternary travertines in co-seismic fissures. *Earth Planet. Sci. Lett.*, **257**, 450–462.

Uysal, T., **Feng, Y.**, **Zhao, J.**, **Isik, V.**, **Nuriel, P.** and **Golding, S.D.** (2009) Hydrothermal CO_2 degassing in seismically active zones during the late Quaternary. *Chem. Geol.*, **265**, 442–454.

Van Noten, K., **Claes, H.**, **Soete, J.**, **Foubert, A.**, **Özkul, M.** and **Swennen, R.** (2013) Fracture networks and strike-slip deformation along reactivated normal faults in Quaternary travertine deposits, Denizli Basin, Western Turkey. *Tectonophysics*, **588**, 154–170.

Vanhaecke, F., **Vanhoe, H.**, **Dams, R.** and **Vandecasteele, C.** (1992) The use of internal standards in ICP-MS. *Talanta*, **39**, 131–142.

Vanhaecke, F., **De Wannemacker, G.**, **Moens, L.** and **Hertogen, J.** (1999) The determination of strontium isotope ratios by means of quadrupolebased ICP-mass spectrometry: a geochronological case study. *J. Anal. At. Spectrom.*, **14**, 1691–1696.

Verrecchia, E.P. and **Verrecchia, K.** (1994) Needle-fiber calcite: critical review and proposed classification. *J. Sediment. Res.*, **64A**, 650–664.

Wang, H., **Yan, H.** and **Liu, Z.** (2014) Contrasts in variations of the carbon and oxygen isotopic composition of travertines formed in pools and a ramp stream at Huanglong Ravine, China: implications for paleoclimatic interpretations. *Geochim. Cosmochim. Acta*, **125**, 34–48.

Westaway, R. (1993) Neogene evolution of the Denizli region of western Turkey. *J. Struct. Geol.*, **15**, 37–53.

Westaway, R., **Guillou, H.**, **Yurtmen, S.**, **Demir, T.**, **Scaillet, S.** and **Rowbotham, G.** (2005) Investigation of the conditions at the start of the present phase of crustal extension in western Turkey, from observations in and around the Denizli region. *Geodin. Acta*, **18**, 209–238.

Yagiz, S. (2006) *Overview on geo-mechanical assessments of Denízlí travertines in Turkey*, IAEG 2006, Paper number 384. The Geological Society of London, 7 pp.

Yagiz, S. (2010) Geomechanical properties of construction stones quarried in South-western Turkey. *Sci. Res. Essays*, **5**, 750–757.

Yan, H., **Sun, H.** and **Liu, Z.** (2012) Equilibrium vs. kinetic fractionation of oxygen isotopes in two low-temperature travertine-depositing systems with differing hydrodynamic conditions at Baishuitai, Yunnan, SW China. *Geochim. Cosmochim. Acta*, **95**, 63–78.

Manuscript received 6 March 2014; revision accepted 12 January 2015

Supporting Information

Additional Supporting Information may be found in the online version of this article:

Appendix S1. Results of stable isotope analysis.

